Physics of the Dark Universe 50 (2025) 102176

Contents lists available at ScienceDirect

Physics of the Dark Universe

journal homepage: www.elsevier.com/locate/dark

Full Length Article

Black holes surrounded by a Murnaghan-fluid scalar gas in a global-monopole background

Y. Sekhmani [a,b,c,d], S. K. Maurya [d,*], J. Rayimbaev [e,f,g,h], Akram Ali [i], M. K. Jasim [d,*], I. Ibragimov [j], S. Muminov [k]

[a] Center for Theoretical Physics, Khazar University, 41 Mehseti Street, AZ1096, Baku, Azerbaijan
[b] Centre for Research Impact & Outcome, Chitkara University Institute of Engineering & Technology, Chitkara University, Rajpura, 140401, Punjab, India
[c] Institute of Nuclear Physics, Ibragimova, 1, Almaty, 050032, Kazakhstan
[d] Department of Mathematical and Physical Sciences, College of Arts and Sciences, University of Nizwa, Nizwa 616, P.O. Box 33, Sultanate of Oman
[e] Urgench State University, Kh. Alimjan Str. 14, Urgench, 221100, Uzbekistan
[f] University of Tashkent for Applied Sciences, Str. Gavhar 1, Tashkent, 100149, Uzbekistan
[g] National University of Uzbekistan, Tashkent, 100174, Uzbekistan
[h] Tashkent State Technical University, Tashkent, 100095, Uzbekistan
[i] Department of Mathematics, College of Sciences, King Khalid University, Abha, 61413, Saudi Arabia
[j] Kimyo International University in Tashkent, Shota Rustaveli street 156, Tashkent, 100121, Uzbekistan
[k] Mamun University, Bolkhovuz Street 2, Khiva, 220900, Uzbekistan

ARTICLE INFO

Keywords:
Black hole
Murnaghan EoS
Global monopole
WKB-Padé approximation

ABSTRACT

We present a detailed comparative analysis of scalar and electromagnetic quasinormal modes (QNMs) for a new static black hole (BH) spacetime solution, which is surrounded by a Murnaghan-type fluid and a global monopole. By combining effective potential diagnostics with Wentzel-Kramers-Brillouin (WKB)-Padé-computed quasinormal mode (QNM) spectra, we demonstrate that the scalar channel whose effective potential contains metric-derivative terms is susceptible to the fluid's nonlinear parameters λ, Γ, β. In this channel, increasing λ or Γ raises and sharpens the photon-sphere barrier, producing higher oscillation frequencies and larger damping rates, while increasing β lowers and broadens the barrier, reducing frequency and prolonging mode lifetimes. The electromagnetic channel, dominated by the centrifugal barrier, i.e., $|g_{tt}|\ell(\ell+1)/r^2$, is comparatively insensitive to derivative-driven fluid structure and instead responds primarily to the monopole parameter η: larger η yields a net redshift that lowers $\mathrm{Re}(\omega)$ and reduces damping, making electromagnetic ringing longer-lived. These complementary sensitivities suggest that combined scalar and electromagnetic spectroscopy can disentangle local fluid stiffness from global redshift effects, with implications for BH stability analyses and potential observational probes of exotic matter surrounding compact objects. In addition, sech-based greybody bounds reveal a consistent relationship with the trends observed in QNM and effective potentials. Specifically, within the parameter ranges examined, it is clear that the strength of the global monopole has a minimal effect on the greybody bounds in the scalar channel.

1. Introduction

In 1915 Albert Einstein formulated *General Relativity* (GR), a geometric theory of gravitation that reconceived gravity as the dynamics of spacetime. One year later Karl Schwarzschild obtained the first nontrivial exact solution of Einstein's field equations, the static spherically symmetric Schwarzschild metric, which was subsequently identified as the archetypal BH solution [1–3]. Black holes (BHs) once regarded as mathematical curiosities have become central objects of both astrophysics and fundamental physics following a succession of observational breakthroughs. Groundbreaking detections of gravitational waves from compact-object coalescences by the LIGO and Virgo Collaborations (beginning with GW150914) provided direct dynamical evidence of BH binaries and their ringdown stages [1]. Complementary electromagnetic probes including radial-velocity surveys that revealed stellar-mass BH candidates [4–6] and the horizon-scale, millimetre-wave images of M87* and Sgr A* delivered by the Event Horizon Telescope (EHT) Collaboration have furnished increasingly direct, model-constraining

* Corresponding author.
E-mail addresses: sekhmaniyassine@gmail.com (Y. Sekhmani), sunil@unizwa.edu.om (S.K. Maurya), javlon@astrin.uz (J. Rayimbaev), akali@kku.edu.sa (A. Ali), mahmoodkhalid@unizwa.edu.om (M.K. Jasim), i.ibragimov@kiut.uz (I. Ibragimov), sokhibjan.muminov@mamunedu.uz (S. Muminov).

https://doi.org/10.1016/j.dark.2025.102176
Received 14 October 2025; Received in revised form 7 November 2025; Accepted 18 November 2025
Available online 24 November 2025

evidence for event-horizon-scale phenomena [7–21]. Strong gravitational lensing in the vicinity of compact objects bends light rays and produces a sharply defined contrast on the observer's sky: the BH shadow. The shadow is determined not by the event horizon itself but by the family of unstable critical null geodesics that separate captured from escaping photons (the photon capture sphere); as a result, the apparent shadow typically subtends an angular size larger than the horizon cross-section [22–25]. Because the shadow boundary is governed by the background spacetime geometry, high-resolution imaging and lensing observables provide a powerful route to measuring BH parameters and to testing GR against alternative theories of gravity [26–36]. In light of these observations, several theoretical studies have undertaken a comparative analysis between the observed data and the theoretical models from a geometrical perspective [37–45].

Complementary to imaging and inspiral measurements, the linear response of compact objects to perturbations encoded in their QNM spectrum captures the dynamical fingerprints of the underlying spacetime. QNMs are damped, characteristic oscillations that arise from perturbations propagating on the exterior geometry; they do not depend on the internal matter content of the BH but rather on the structure of the spacetime outside the horizon. Mathematically, QNMs appear as complex eigenfrequencies whose real parts determine oscillation frequencies and whose imaginary parts set exponential decay rates; they are obtained by imposing purely ingoing boundary conditions at the horizon and purely outgoing conditions at spatial infinity (or the appropriate asymptotic region), yielding a discrete set of complex frequencies. The ringdown observed in gravitational-wave signals after a merger (e.g. GW150914) is well described by the dominant QNMs of the remnant, making their accurate computation essential for precision tests of GR and for probing possible deviations from the Kerr paradigm [46]. Except for a few exceptional cases, QNM frequencies cannot be obtained in closed form and must be computed numerically or semi-analytically. A diverse arsenal of techniques including WKB and Padé methods, the continued-fraction (Leaver) method, the asymptotic iteration method (AIM), time-domain integration, and matrix- or spectral -based approaches-has been developed to obtain highly accurate spectra for scalar, electromagnetic, gravitational and higher-form perturbations [47,48]. Extensive investigations have explored QNMs across a wide range of spacetimes, including higher-dimensional geometries and a variety of modified gravity models, revealing rich structure and guiding observational strategies to constrain fundamental physics from ringdown and stability analyses [49–64].

Topological defects such as global monopoles further enrich the spectrum of BH geometries. global monopoles arise from the spontaneous breaking of a global SO(3) symmetry and imprint a solid-angle deficit on the ambient spacetime, thereby modifying geodesic structure, light deflection and horizon properties [65–67]. The original gravitational field of a global monopole was analysed by Barriola and Vilenkin [65], while subsequent work highlighted nontrivial features such as repulsive gravitational effects and the role of nonminimal couplings [68,69]. Both ordinary global monopoles, endowed with canonical (positive) kinetic energy, and phantom global monopoles, characterised by negative kinetic terms that violate standard energy conditions, have been extensively investigated in a variety of settings [70,72]. Embedding monopoles into BH backgrounds produces a versatile theoretical laboratory for probing departures from the predictions of GR: the modified causal structure and effective potentials affect lensing observables, thermodynamic properties and the spectrum of linear perturbations [71,73,74]. In particular, vacuum-polarisation and field-decay effects in monopole spacetimes have been studied in detail [75,76], and recent analyses have examined greybody factors and QNM spectra for BHs threaded by global monopoles [77]. Collectively, these works motivate the systematic study performed here of a four-dimensional BH surrounded by a global monopole and a Murnaghan-type effective fluid, with the aim of quantifying the observational imprint on QNMs and greybody factors.

The Murnaghan equation of state (EoS), originally introduced in solid-state physics to characterise the pressure-volume response of crystalline media under compression, provides a simple yet flexible phenomenological relation between pressure and density that has found renewed application in cosmology and gravitation [78,79]. Recently a double-polytropic reinterpretation of the Murnaghan EoS has been proposed for cosmology: when regarded as the superposition of two polytropic constituents the model can emulate a cosmological constant together with logotropic or generalized Chaplygin-type behaviour, approximating the background expansion of ΛCDM while allowing novel perturbation dynamics [80]. Motivated by this versatility, in the present work we adopt the Murnaghan ansatz

$$P(\rho) \;=\; -\beta\,\rho \;-\; \lambda\,\rho^{\,1+\frac{1}{\Gamma}},$$

with β, λ, Γ constant parameters controlling the linear (vacuum-like) and nonlinear (polytropic) contributions. This form can be viewed as a nonlinear generalisation of the standard polytropic law $P \propto \rho^{1+1/\Gamma}$: in the small-strain limit the nonlinear term reduces to a pure power law, while owing to Murnaghan's phenomenological choice for the bulk modulus the ansatz remains well behaved for finite density excursions without invoking an infinite series of higher-order corrections [78,79]. Embedded as an effective exterior (or near-horizon) fluid surrounding a four-dimensional BH endowed with a global monopole, the Murnaghan model provides a controlled, two-parameter deformation of the background stress-energy that is ideally suited for systematic studies of linear response: QNM spectra (probing exterior geometry and stability) and greybody factors (sensitive to the near-horizon effective potential) can both be computed and contrasted with vacuum or simple perfect-fluid limits to quantify the observable imprint of the Murnaghan fluid on ringdown and radiative transfer [80].

To situate our Murnaghan and monopole construction within the rapidly developing literature on compact objects with exotic matter and topological defects, such that the recent analysis in [81] provides useful examples of special-function metric structures and their imprint on QNM spectra. The closely related work [82] studies Murnaghan-like equations of state coupled to topological defects and thereby offers a direct point-by-point comparison to our source construction. Ref. [83] explores lensing and near-horizon observables for wormhole- and defect-like geometries, highlighting astrophysical diagnostics that can complement our greybody and QNM-based probes. Two recent studies [84,85] analyse monopole-induced redshifts and their effects on particle motion, perturbations and greybody factors, which are relevant for interpreting the electromagnetic-channel sensitivity we report. Ref. [86] provides a detailed treatment of Dirac/field perturbations and greybody radiation in regular BH backgrounds and supplies useful techniques for our sparsity and emission-rate estimates. Ref. [87] develops recent theoretical perspectives on nonlinear-fluid sourcing of compact objects and helps to place our Murnaghan parametrisation in a broader modelling framework. Finally, the fluid-dynamics study in [88] examines properties of the Tait/Murnaghan family relevant to cavitation and singularity formation and informs our assessment of physical plausibility and parameter ranges for the Murnaghan sector. On the other hand, the static-fluid BH solutions and anisotropic-fluid analyses of [89] supply precedent for matching exterior analytic solutions to plausible interior cores and motivate the matching conditions we discuss. In a broader theoretical context, recent studies on Lorentzian Euclidean BHs and quantum modified geometries [90–93] have shown that causal structure transitions, atemporality, and effective quantum corrections can regularise singularities and alter key observables such as shadows and accretion dynamics. These developments provide a complementary framework to the present Murnaghan monopole BH solution, where the combined effects of nonlinear fluid stiffness and topological charge similarly reshape the near-horizon geometry and radiative properties, offering a unified setting to investigate departures from classical Schwarzschild behaviour. Moreover, the possible detection of distinctive gravitational or analogue signatures such as gravitational wave echoes and modifications in ring-

down spectra has emerged as an exciting avenue for probing nonstandard horizon physics and matter couplings [94–97]. In this context, exploring such effects within the framework of the proposed Murnaghan-monopole BH may provide valuable insights into how nonlinear fluid stiffness and topological charge imprint themselves on the dynamical and radiative behaviour of compact objects.

In this work we extend the above developments by constructing and analysing an exact BH solution within the framework of GR. The spacetime is sourced by two novel ingredients: (i) an effective scalar gas described by the Murnaghan EoS, which furnishes a dark energy mimicking negative pressure component, and (ii) a topological defect modelled by a global monopole arising from the spontaneous breaking of an SO(3) symmetry. The combined presence of a global monopole and a Murnaghan fluid generates controlled deformations of the exterior stress-energy tensor and of the geodesic structure, thereby providing a rich but tractable setting to investigate both the static gravitational background and its dynamical linear response (ringdown and scattering) properties.

The paper is organised as follows. In Section 2 we present the theoretical setup: the action and field equations, the ansatz for the global monopole scalar field and its energy-momentum tensor, and the Murnaghan ansatz for the surrounding scalar gas. Section 3 is devoted to solving the Einstein equations for the combined source and to deriving an exact analytical expression for the Murnaghan fluid energy density; we then analyse the pointwise energy conditions and extract the resulting metric function. Section 4 computes the Hawking temperature and performs a quantitative study of Hawking-radiation sparsity for the obtained BH. Section 5 addresses the linear stability and dynamical response: we derive the master wave equations for scalar and electromagnetic perturbations and compute QNM spectra using a Padé-resummed WKB approach (third-order Padé), emphasising the distinct imprints of the Murnaghan fluid and the monopole defect on the ringdown frequencies and damping rates. Section 6 examines scattering and radiative transfer by computing greybody factors for electromagnetic perturbations and analysing their dependence on the model parameters. Finally, Section 7 summarises the principal results and discusses prospects for extensions, including rotating generalisations, alternative matching prescriptions for the effective fluid, and observational signatures that could constrain the Murnaghan parameters and the monopole charge.

2. Global monopole defect coupled to scalar gas model of dark energy with Murnaghan EoS: $p = -(\beta + \lambda\rho^{1+\frac{1}{\Gamma}})$

To establish a self-consistent framework for scalar-field gases in GR, we begin from an action principle in four spacetime dimensions. The gravitational dynamics are governed by the Einstein-Hilbert term, while the matter sector is composed of two parts: (i) a global monopole triplet ϕ^a, and (ii) an effective contribution $\mathcal{S}_{\rm Mur}$ whose on-shell stress tensor reproduces the Murnaghan EoS. The total action then reads

$$S = \int d^4x\,\sqrt{-g}\left[\frac{\mathcal{R}}{2\kappa} + \mathcal{L}_{\rm GM}\right] + S_{\rm Mur}, \tag{1}$$

where $\mathcal{R}$ is the Ricci scalar, $g = \det(g_{\mu\nu})$ is the determinant of the metric tensor[1], and the global-monopole Lagrangian is

$$\mathcal{L}_{\rm GM} = -\tfrac{1}{2}\,g^{\mu\nu}\partial_\mu\phi^a\partial_\nu\phi^a - \frac{\lambda}{4}\left(\phi^a\phi^a - \eta^2\right)^2, \qquad a = 1,2,3\,. \tag{2}$$

Here η sets the symmetry-breaking scale and $\lambda > 0$ controls the monopole core size. Indeed, η sets the scale of spontaneous breaking of the global $O(3)$ symmetry down to $O(2)$ [109,110]. In the familiar four-dimensional case one typically chooses $\eta \sim 10^{16}\,\text{GeV} \simeq M_P = \ell_P^{-1}$, with M_P and ℓ_P the Planck mass and length, respectively [111]. More generally, dimensional analysis in four spacetime dimensions implies that η carries mass dimension one but is bounded by the natural short-distance cutoff set by the four-dimensional Planck scale: $\eta \lesssim \ell_P^{-1}$.

[1] In the following, we assume that $\kappa = 8\pi G = c = 1$, where G and c are, respectively, the Newtonian gravitational constant and the speed of light.

By varying the action (1) with respect to the metric tensor $g_{\mu\nu}$, we obtain the corresponding gravitational field equations:

$$\mathcal{I}_{\mu\nu} = \mathcal{R}_{\mu\nu} - \frac{1}{2}g_{\mu\nu}\mathcal{R} - \kappa\left(\mathcal{T}^{\rm GM}_{\mu\nu} + \mathcal{T}^{\rm Mur}_{\mu\nu}\right) = 0, \tag{3}$$

where $\mathcal{T}\mu\nu^{\rm GM}$ and $\mathcal{T}\mu\nu^{\rm Mur}$ denote the energy-momentum tensors associated with the global monopole charge and the matter sector described by a Murnaghan-type EoS, respectively. To aid in the analysis of the field equations, we will initially concentrate on the global monopole charge sector, the energy-momentum tensor associated with the global monopole configuration, which arises from the variation of the underlying action functional with respect to $g^{\mu\nu}$, is supplemented by the dynamical equation of the scalar field expressed in the following explicit form:

$$\mathcal{T}_\mu^{\nu\,\rm GM} = \partial_\mu\phi^a\partial^\nu\phi^a - \delta^\nu_\mu\left(\frac{1}{2}(\partial\phi^a)^2 + \mathcal{V}(\phi^2)\right) \tag{4}$$

$$\Box\phi^a = \frac{\partial\mathcal{V}}{\partial\phi^a}. \tag{5}$$

To model an exact BH solution in four-dimensional gravitational framework, we consider a static and spherically symmetric spacetime, where the temporal and radial components of the metric are related by the simplifying condition, $g_{tt}\,g_{rr} = -1$. This leads to the following canonical form of the line element:

$$\mathrm{d}s^2 = g_{\mu\nu}\mathrm{d}x^\mu\mathrm{d}x^\nu = -F(r)\,\mathrm{d}t^2 + \frac{\mathrm{d}r^2}{F(r)} + r^2\,\sin^2\theta\,\mathrm{d}\phi^2 + r^2\,\mathrm{d}\theta^2, \tag{6}$$

where $F(r)$ is the metric function to be determined, encoding the gravitational dynamics of the spacetime.

We consider a static, spherically symmetric spacetime minimally coupled to an anisotropic fluid, whose energy-momentum tensor is expressed as

$$\mathcal{T}_{\mu\nu} = (\rho + p_t)u_\mu u_\nu + p_t g_{\mu\nu} + (p_r - p_t)\chi_\mu\chi_\nu, \tag{7}$$

where ρ denotes the energy density, and p_r and p_t correspond to the radial and tangential pressures, respectively. The four-velocity of the fluid is represented by u^μ, while χ^μ is a unit spacelike vector field orthogonal to u^μ, capturing the anisotropic nature of the pressure distribution. These vector fields obey the normalization and orthogonality conditions $u^\mu u_\mu = -1$, $\chi^\mu\chi_\mu = 1$, and $u^\mu\chi_\mu = 0$, thereby ensuring the physical consistency of the fluid description within the spacetime geometry. This general anisotropic structure extends the usual perfect fluid description and is capable of modeling dark energy configurations with directional pressure disparities due to strong curvature effects. Anisotropies are known to emerge naturally in a wide range of contexts, including in the presence of magnetic fields, phase transitions, or quantum fields in curved backgrounds [112–114].

In the comoving frame with $u^\mu = \sqrt{F(r)}\,\delta^\mu_0$ and $\chi^\mu = 1/\sqrt{F(r)}\,\delta^\mu_1$, the mixed components of the energy-momentum tensor reduce to $\mathcal{T}^\mu_\nu = \mathrm{diag}(-\rho, p_r, p_t, \ldots, p_t)$, clearly displaying the anisotropic nature of the stress distribution.

Rather than adopting the standard barotropic relation $p = \omega\rho$, we employ a nonlinear EoS inspired by the Murnaghan form [78]:

$$p(\rho) = -\beta\rho - \lambda\rho^{1+\frac{1}{\Gamma}}, \tag{8}$$

where the constants $\beta > 0$, $\lambda > 0$, and $\Gamma > 0$ are model parameters. This EoS mimics a dark energy fluid with a pressure more negative than that of a cosmological constant, corresponding to a phantom-like regime [117,118].

The form (8) generalizes the linear phantom fluid model ($p = \omega\rho$ with $\omega < -1$) and introduces nonlinear corrections relevant in high-density regimes, possibly arising from quantum gravity effects or exotic matter configurations. It is also consistent with recent effective field theory descriptions of dark energy fluids in strongly curved spacetimes [119,120].

In Schwarzschild-like spacetimes, the radial coordinate becomes temporal inside the event horizon. To maintain regularity and continuity across the horizon, we impose the constraint

$$p_r = -\rho, \tag{9}$$

which guarantees that the energy density remains invariant under $r \leftrightarrow t$ coordinate exchange. This condition has been employed in several models of anisotropic dark energy accretion and BH interiors [119,130].

To relate the tangential pressure p_t to the averaged isotropic pressure p obeying the Murnaghan EoS, we use the angular averaging condition

$$p = p_t + \frac{1}{3}(p_r - p_t), \tag{10}$$

which arises from projecting the energy-momentum tensor on an angular hypersurface: $\langle \delta_i^1 \delta_1^j \rangle = 1/3$. Substituting Eq. (9) and the EoS (8) into Eq. (10), we find

$$p_t = \frac{1}{2}\left((1-3\beta)\rho - 3\lambda\rho^{1+\frac{1}{\Gamma}}\right). \tag{11}$$

The final expressions for the nonzero mixed components of the energy-momentum tensor are:

$$\mathcal{T}_t^t = \mathcal{T}_r^r = -\rho, \tag{12}$$

$$\mathcal{T}_{\theta_i}^{\theta_i} = p_t = \frac{1}{2}\left((1-3\beta)\rho - 3\lambda\,\rho^{1+\frac{1}{\Gamma}}\right). \tag{13}$$

These expressions ensure that the effective fluid exhibits repulsive gravitational behavior and anisotropy consistent with a phantom dark energy model. The degree of anisotropy is determined by the deviation of p_t from $p_r = -\rho$ and is controlled by the parameters μ, λ, and ξ. The condition $p_t > p_r$ can lead to dynamical instabilities or exotic horizon structures, while $p_t < p_r$ may support stable compact configurations depending on boundary conditions [112,114].

3. Exact solutions

The study of a precise BH solution requires looking at the equations that describe gravity and matter (3). By considering static and spherically symmetric features (6), one finds that $\mathcal{T}_t^t = \mathcal{T}_r^r$. Consequently, the gravitational framework can be modeled in higher-dimensional spacetime through the following field equations:

$$\mathcal{I}_t^t = \mathcal{I}_r^r = \frac{1}{r^2}(F(r)-1) + \frac{1}{r}F'(r), \tag{14}$$

$$\mathcal{I}_\theta^\theta = \mathcal{I}_\phi^\phi = \frac{F''(r)}{2} + \frac{F'(r)}{r}. \tag{15}$$

At this juncture, it may be beneficial to adopt a more thorough approach by examining the matter sector associated with non-linear electrodynamics, global monopoles, and the matter fluid using the Murnaghan EoS. In this way, global monopole configurations within GR can be treated in terms of the Higgs profile $\gamma(r)$ and the metric spacetime elements, which embrace no exact exterior solution and ought to be integrated numerically. Nonetheless, because the scalar field eventually approaches its vacuum expectation value (VEV) outside a core of radius $\delta \sim \eta^{-1} \ll r_h$. In addition, the thin-core approximation may be used when the energy density in the outer area scales as $\rho \sim \eta^2/r^2$ [65,121]. For $r \geq \delta$ (and thus outside the horizon at r_h), one set $\gamma(r) = 1$ and $\mathcal{V}(\phi^a) = 0$, so that the stress-energy tensor reduces to

$$T_\mu^{\nu\,GM} = \left\{T_0^0, T_1^1, T_\theta^\theta, T_\phi^\phi\right\} = \left\{-\frac{\eta^2}{r^2}, -\frac{\eta^2}{r^2}, 0, 0\right\} \tag{16}$$

yielding a spacetime with a solid-angle deficit but no Newtonian gravitational attraction [65,122]. The numerical interior solution for $r < \delta$ is then matched at $r \approx \delta$ to this analytic exterior form, ensuring continuity of the metric and its first derivatives across the core boundary [123,124].

Finding exact analytical solutions in GR requires simultaneously satisfying the gravitational and matter field Eq. (3). This condition is equivalent to enforcing energy-momentum conservation through the contracted Bianchi identity, $T^{\mu\nu}{}_{;\nu} = 0$, which reduces to the fluid continuity equation in a static, spherically symmetric background [125,126]. Incorporating the Murnaghan-type EoS (8) leads directly to a first-order radial ordinary differential equation governing the fluid dynamics such that

$$r\,\rho'(r) + 3\,\rho - 3\left(\beta\,\rho + \lambda\,\rho^{1+\frac{1}{\Gamma}}\right) = 0, \tag{17}$$

which integrates to the closed-form density profile

$$\rho(r) = \left(\frac{\lambda + \chi^2 r^{-\frac{3(\beta-1)}{\Gamma}}}{1-\beta}\right)^{-\Gamma}, \tag{18}$$

where χ is an integration constant. The integration constant χ that appears in the analytic density profile (18) parametrizes the amplitude of the radius-dependent (nonlinear) component of the Murnaghan fluid and therefore sets the characteristic radius r_c (Eq. (19)) which separates the inner, nonlinear core from the asymptotic, vacuum-like regime. Physically, χ controls how strongly the nonlinear (power-law) piece of the density contributes at moderate radii: larger χ increases the relative importance of the inner core term $\propto \chi^2 r^{-3(\beta-1)/\Gamma}$ and therefore pushes the region of substantial fluid backreaction outward. From a matching perspective χ is fixed once an interior/core model is chosen (for example by matching the analytic exterior to a numerical monopole core solution at $r \simeq \delta$ by imposing continuity of the metric and its first derivative), or equivalently by imposing an asymptotic normalization condition such as a specified $\rho(r \to \infty)$ or a finite fluid mass

$$M_{\rm fluid} = 4\pi \int_{r_h}^{\infty} \rho(r;\chi)\, r^2\, dr,$$

which can be inverted numerically to determine χ. In practice we therefore treat χ either via a physically motivated interior–exterior matching or phenomenologically as a parameter constrained by the energy-condition and stability bounds discussed in Section 3.

For $r \ll r_c = [(1-\beta)\chi^2/\lambda]^{\Gamma/[3(\beta-1)]}$, the core scales as $\rho \propto r^{3(\beta-1)}$; as $r \to \infty$, $\rho \to [\lambda/(1-\beta)]^{-\Gamma}$. In this framework, χ emerges as an integration constant from the continuity equation, encapsulating the amplitude of the nonlinear density component within $\rho(r)$. A closer inspection reveals that for radial distances much smaller than the characteristic scale r_c,

$$r \ll r_c = \left[\frac{(1-\beta)\chi^2}{\lambda}\right]^{\frac{1}{\zeta}}, \quad \text{where} \quad \zeta = \frac{3(\beta-1)}{\Gamma}, \tag{19}$$

the nonlinear term $\chi^2 r^{-\zeta}$ overwhelmingly dominates over the constant λ. This dominance shapes a steep core density profile $\rho(r) \propto r^{3(\beta-1)}$, which is characteristic of anisotropic fluid configurations in higher-dimensional spacetimes [125–127]. Such a profile reflects strong nonlinear effects governing the inner regions.

Conversely, in the asymptotic regime $r \to \infty$, the constant term γ becomes dominant, causing the density to approach a constant value

$$\rho_\infty = \left[\frac{\lambda}{1-\beta}\right]^{-\xi}, \tag{20}$$

which acts effectively as a vacuum energy component driving late-time cosmic acceleration, akin to dark energy [117,118]. For the model to remain physically meaningful, positivity and regularity impose the constraints $\lambda > 0$ and $1 - \beta > 0$. Furthermore, entering the phantom regime where $\beta > 1$ (equivalently, an EoS parameter $\omega = p/\rho < -1$) results in a mild violation of the null energy condition, in line with scenarios of phantom energy accretion onto BHs [119]. Therefore, this analytic density profile of the Murnaghan type provides a unified description that smoothly interpolates between a nonlinear, steeply varying core and a dark-energy-like vacuum exterior, explicitly realized here in four spatial dimensions. This unification offers a valuable tool for modeling anisotropic fluids in four-dimensional gravitational settings with applications to both astrophysical objects and cosmology.

On the other hand, the Murnaghan fluid density approaches a constant $\rho_\infty = \left(\frac{\lambda}{1-\beta}\right)^{-\xi}$ at large radii, yielding asymptotic pressures

$$p_{r,\infty} = -\beta\,\rho_\infty - \lambda\,\rho_\infty^{1+\frac{1}{\xi}}, \quad p_{t,\infty} = \frac{1}{2}\left(3p_\infty - p_{r,\infty}\right), \tag{21}$$

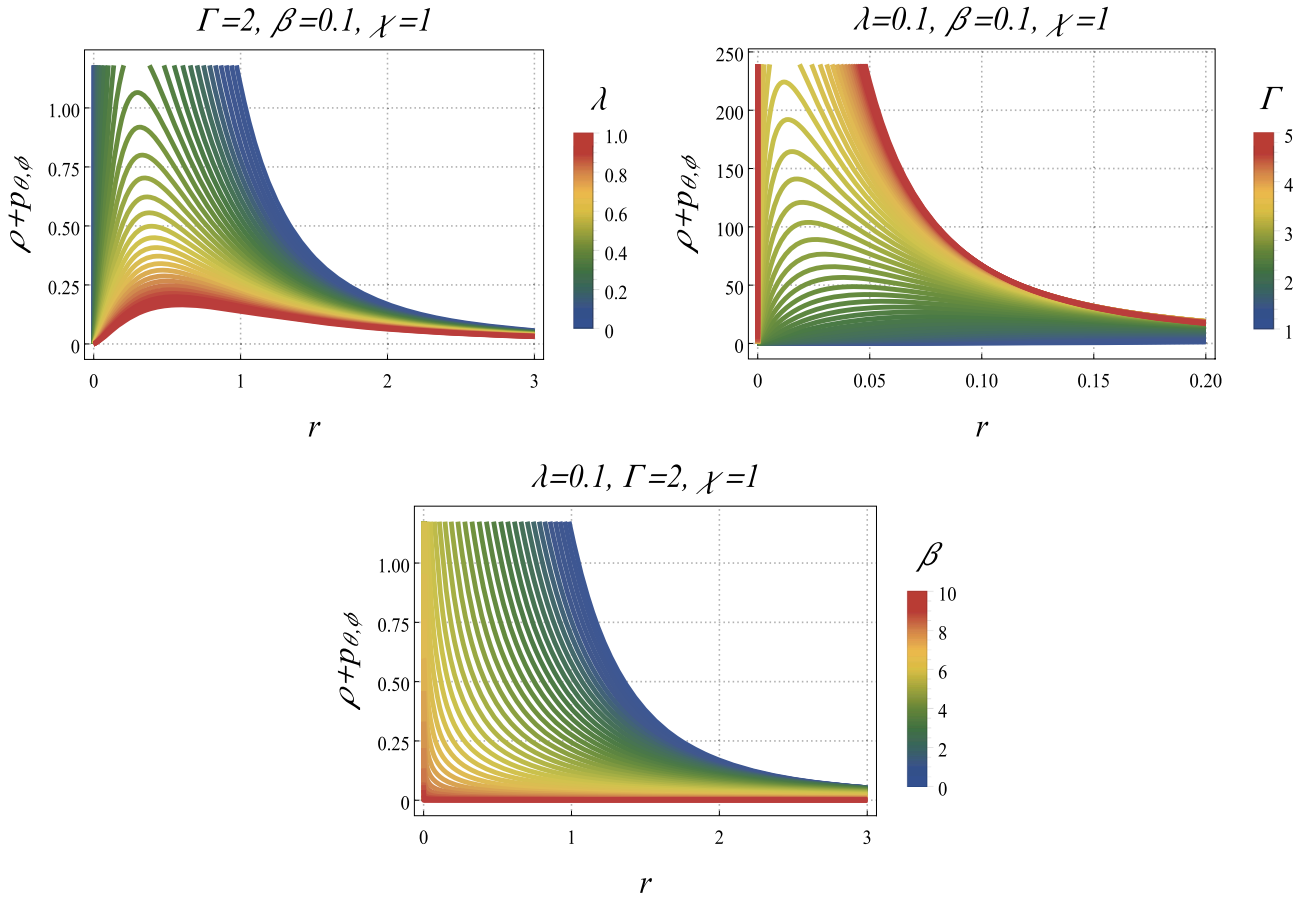

Fig. 1. The variation of $\rho + p_{\theta,\phi}$ (NEC) against r for multiple values of the Murnaghan parameter sector.

with $p_\infty = p_{r,\infty}$. The anisotropy factor $\Delta_\infty = p_{t,\infty} - p_{r,\infty}$ vanishes at leading order under the fine-tuned condition $\lambda = (1-\beta)\rho_\infty^{-1/\xi}$, indicating asymptotic isotropy. Nonetheless, subleading corrections and inhomogeneities may induce small residual anisotropies, distinguishing Murnaghan fluids from quintessential or constant-density dark energy models where anisotropy typically disappears. Such anisotropic stresses could leave observable imprints on cosmic expansion and structure formation, motivating further exploration of Murnaghan-type nonlinear fluids in cosmology.

To gain clearer insight into the physical properties of our solution, we now examine the classical energy conditions (ECs), the null energy condition (NEC), dominant energy condition (DEC), weak energy condition (WEC), and strong energy condition (SEC) which are defined as follows [131]:

$$\begin{aligned}
&\textbf{WEC}: \rho \geq 0, \quad \rho + P_i \geq 0, \textbf{SEC}: \rho + \sum_i P_i \geq 0, \quad \rho + P_i \geq 0, \\
&\textbf{NEC}: \rho + P_i \geq 0, \textbf{DEC}: \rho \geq 0, \quad |P_i| \leq \rho.
\end{aligned} \tag{22}$$

Thus, complete expressions may be provided as follows:

$$\begin{aligned}
&\rho + p_r = 0, \qquad \rho + p_{\theta,\phi} = \frac{3}{2}\left[\rho(1-\beta) - \lambda\,\rho^{1+\frac{1}{\Gamma}}\right], \\
&\rho + \sum_i p_i = \rho\left(1 - \frac{3\beta}{2}\right) - \frac{3}{2}\lambda\,\rho^{1+\frac{1}{\Gamma}}, \\
&\rho - |p_r| = 0, \qquad \rho - |p_{\theta,\phi}| = \rho - \left|\frac{\rho}{2}(1-3\beta) - \frac{3}{2}\lambda\,\rho^{1+\frac{1}{\Gamma}}\right|.
\end{aligned} \tag{23}$$

Investigating the ECs according to the exact solution for the energy density (18) yields the following explicit expressions:

$$\begin{aligned}
\rho + P_{\theta,\phi} &= -\frac{3(\beta-1)\chi^2}{2\left(\lambda\, r^{\frac{3(\beta-1)}{\Gamma}} + \chi^2\right)}\left(\frac{\lambda + \chi^2 r^{-\frac{3(\beta-1)}{\chi}}}{1-\beta}\right)^{-\Gamma}, \\
\rho + \sum_i P_i &= \left(\frac{\lambda + \chi^2 r^{-\frac{3(\beta-1)}{\Gamma}}}{1-\beta}\right)^{-\Gamma}\left[\beta(1-4) - \frac{(1-\beta)\lambda\cdot 3}{\lambda + \chi^2 r^{-\frac{3(\beta-1)}{\Gamma}}} + 1\right], \\
\rho - |P_{\theta,\phi}| &= \frac{1}{2}\left(\frac{\lambda + \chi^2 r^{-\frac{3(\beta-1)}{\Gamma}}}{1-\beta}\right)^{-\Gamma}\left[-\beta(1+4) + \frac{(1-\beta)\lambda\cdot 3}{\lambda + \chi^2 r^{-\frac{3(\beta-1)}{\Gamma}}} + 1\right].
\end{aligned} \tag{24}$$

To assess the classical energy conditions, we define $B(r) \equiv \lambda + \chi^2 r^{-k}/(1-\beta)$ with $k = 3(\beta-1)/(\Gamma)$, so that $\rho(r) = B(r)^{-\Gamma}$. The radial combination is identically saturated, $\rho + p_r = 0$, while the tangential combination factorises as $\rho + p_{\theta,\phi} = \frac{3}{2}B^{-(\Gamma+1)}\chi^2 r^{-k}$, which is strictly positive for $B(r) > 0$ and $\chi^2 > 0$; hence the NEC (and therefore the WEC) is satisfied wherever $B(r) > 0$. The DEC is marginal in the radial direction since $|p_r| = \rho$, whereas the tangential DEC requires $-1 \leq 1/2(1 - 3\beta - 3/\lambda\,\rho^{1/\Gamma}) \leq 1$, an inequality that for small or vanishing λ reduces to $|1-3\beta| \leq 2$ (i.e., $-1/3 \leq \beta \leq 1$). Finally the SEC reduces to the algebraic condition $B\left(1 - 3/2\beta\right) \geq 3/2\lambda$, which for $\lambda = 0$ implies $\beta \leq 2/3$. In practice, a physically admissible and simple parameter choice that guarantees $\rho > 0$ and that the NEC/WEC hold everywhere is $\beta < 1$, $\Gamma > 0$, $\chi^2 > 0$ with $\lambda \gtrsim 0$, while DEC and SEC impose the additional mild parameter constraints displayed above (these must be checked explicitly if λ is large or $\beta \geq 1$).

Fig. 1 display the combination $\rho + p_{\theta,\phi}$ as a function of the areal radius r for representative choices of the Murnaghan parameters

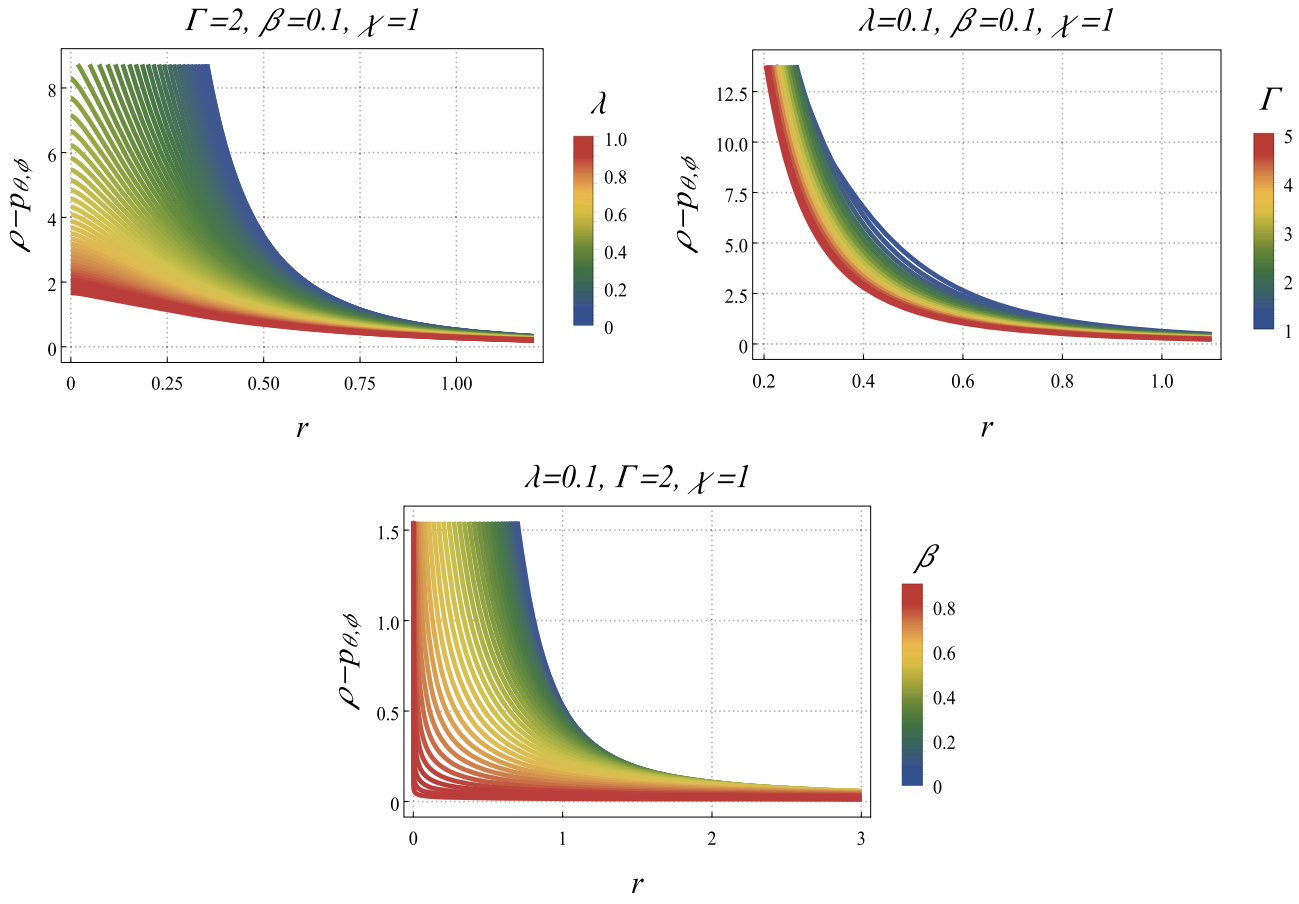

Fig. 2. The variation of $\rho - p_{\theta,\phi}$ (DEC) against r for multiple values of the Murnaghan parameter sector.

$(\lambda, \beta, \Gamma, \chi)$. Across the shown slices, the NEC is satisfied at sufficiently large r, but $\rho + p_{\theta,\phi}$ can become negative in the near-horizon region, depending on the choice of Murnaghan sector parameters. Physically, this stems from the fact that the Murnaghan scalar fluid adds terms whose radial scaling is controlled by β and Γ; increasing β (within the sub-phantom window considered here) amplifies the scalar-= fluid contribution at intermediate radii, thereby raising the likelihood of NEC violation close to the BH horizon.

Fig. 2 illustrates the quantity $\rho - p_{\theta,\phi}$, which is associated with DEC, for the same representative parameters as observed in the NEC behaviours. The qualitative behaviour is similar to that of Fig. 1, but with a somewhat more restrictive outcome: the DEC is violated over broader regions of parameter space whenever the Murnaghan fluid induces large negative transverse pressures. In particular, decreasing the stiffness parameter λ or increasing the nonlinearity parameter β (at fixed Γ) drives $\rho - p_{\theta,\phi}$ more negative in the near-horizon regime, since the nonlinear pressure term grows in magnitude and undergoes sign changes more rapidly. This demonstrates that the DEC imposes tighter bounds on the Murnaghan sector compared to the NEC, particularly when strong near-horizon scalar fluid effects are present.

Fig. 3 illustrates the SEC behaviour against r, emphasising its notable sensitivity to both the Murnaghan exponent and the nonlinear parameters. Among the three classical conditions, the SEC is found to be the most fragile when interacting with the Murnaghan scalar fluid, as the contributions from scalar pressure can readily turn negative. Quantitatively, for the parameter choices presented, there are extended intervals in radius where the SEC is violated, especially when the nonlinearity parameter β is increased or when the exponent Γ assumes values that enhance the hypergeometric correction. This behaviour suggests that the SEC is often the first of the standard energy conditions to be violated, highlighting the considerable impact of scalar induced pressures on the Murnaghan sector.

At this advanced stage, having derived exact solutions for the matter sector, we proceed to construct the exact analytical BH solution by carefully analyzing the full set of gravitational field equations. These equations, expressed in terms of the metric function $F(r)$, the cosmological constant Λ, the Yang-Mills magnetic charge Q, and the matter energy density $\rho(r)$, read explicitly as follows:

$$\mathcal{I}_t^t = \mathcal{I}_r^r = \frac{F(r)-1}{r^2} + \frac{F'(r)}{r} + \frac{\eta}{r^2} + \rho(r), \tag{25}$$

$$\mathcal{I}_\theta^\theta = \mathcal{I}_\phi^\phi = \frac{F''(r)}{2} + \frac{F'(r)}{r} + \frac{\eta}{r^2} + \frac{1-3\beta}{2}\rho(r) + \frac{3}{2}\lambda\,\rho^{1+\frac{1}{\Gamma}}. \tag{26}$$

By substituting the energy density $\rho(r)$ derived from the nonlinear Murnaghan EoS (18) into the temporal component $\mathcal{I}_t^t$, we obtain a nonlinear differential equation governing $F(r)$. Remarkably, this equation admits an exact closed-form solution given by

$$F(r) = 1 - \frac{2M}{r} - 8\pi\eta^2 - \frac{1}{3}r^2\left(\frac{1-\beta}{\lambda}\right)^{\Gamma} {}_2F_1\left(\Gamma, \frac{\Gamma}{1-\beta}; \frac{\Gamma}{1-\beta}+1; -\frac{r^{-\frac{3(\beta-1)}{\Gamma}}\chi^2}{\lambda}\right). \tag{27}$$

Here, M represents the ADM mass, the hypergeometric function ${}_2F_1(a_1, a_2; a_3; a_4)$ emerges naturally as the solution to the underlying hypergeometric differential equation. It converges for $|a_4| < 1$ and admits the well-known power series expansion

$${}_2F_1(a_1, a_2; a_3; a_4) = \sum_{p=0}^{\infty} \frac{(a_1)_p (a_2)_p}{(a_3)_p} \frac{a_4^p}{p!},$$

where $(a)_p = a(a+1)\cdots(a+p-1)$ is the Pochhammer symbol (rising factorial) with $(a)_0 = 1$. This function frequently appears in mathemati-

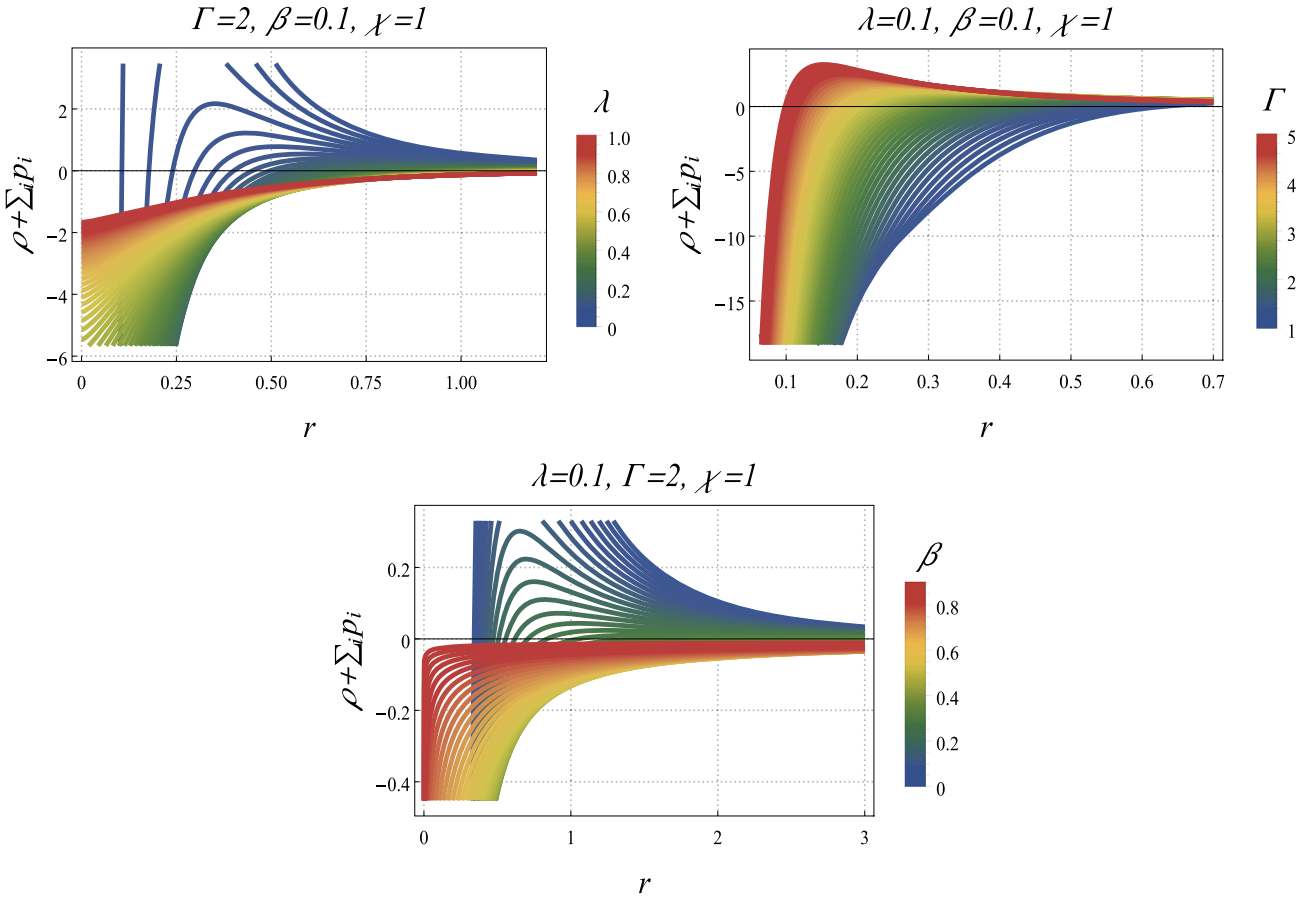

Fig. 3. The variation of $\rho + \sum_i p_i$ (SEC) against r for multiple values of the Murnaghan parameter sector.

cal physics and GR when solving second-order linear differential equations with three regular singular points [128]. The Gauss hypergeometric function appearing in Eq. (27) is a direct consequence of integrating source terms that contain non-integer power-law combinations typical of the Murnaghan equation of state; structurally one encounters integrals of the form $\int r^p(1 + Ar^q)^s\, dr$ with non-integer s, whose primitives reduce to ${}_2F_1$-type expressions after a suitable change of variables. In the present solution the hypergeometric argument is controlled by the dimensionless combination $\chi^2 r^{-3(\beta-1)/\Gamma}/\lambda$, which means that variations in $\{\beta, \Gamma, \lambda, \chi\}$ do not merely rescale prefactors but shift the analytic structure (series coefficients, branch points and radius of convergence) of the metric function. This contrasts mildly with many nonlinear-electrodynamics or anisotropic-fluid solutions where special functions appear but with arguments and coefficients tied to different physical fields; in those models the special-function dependence often encodes electromagnetic nonlinearity or dual-power profiles [115,116].

A deeper analysis of the obtained BH solution shows that the global monopole parameter η and the Murnaghan parameters (β, λ, Γ) play distinct and complementary roles in shaping the causal structure. The global monopole manifests primarily as a solid-angle deficit, encoded through the asymptotic angular prefactor α_∞, which decreases below unity when $\eta \neq 0$. This effect does not create additional horizons but shifts the location of the outer horizon outward, thereby enlarging the BH radius and increasing its area. In contrast, the Murnaghan parameters govern the nonlinear scalar fluid contribution to the stress-energy tensor, modifying the radial dependence of the metric function $F(r)$. The parameter λ acts as a regulator that stiffens the effective fluid: large λ suppresses nonlinear corrections and drives the geometry toward Schwarzschild-like behavior with a single horizon, whereas small λ amplifies nonlinear terms, enlarging the outer horizon. The exponent Γ controls the shape of the nonlinear term, with larger Γ redistributing the scalar fluid corrections toward the core and altering the slope of $F(r)$ near the horizon. Finally, the phantom-like coupling β has the strongest effect on the inner profile: larger β deepens the intermediate potential well of $F(r)$ and can generate exotic behaviors, but within the physical window $\beta < 1$ the solution remains regular and Schwarzschild-like. Together, these results confirm that η dictates global geometric deformations, while (β, λ, Γ) govern local nonlinear modifications of the horizon and near-horizon structure.

Fig. 4 illustrates these effects explicitly by displaying the metric function $F(r)$ for different slices of parameter space. In the λ-panel, the geometry remains Schwarzschild-like with a single horizon across the entire range: increasing λ decreases the horizon radius, while decreasing λ enlarges it. The β-panel demonstrates that variations in the phantom coupling reshape the near-horizon slope of $F(r)$: higher β reduces the height of the curve and shifts the crossing point inward, although within the non-phantom regime no inner horizon emerges. The Γ-panel shows that increasing Γ modifies the overall amplitude of the hypergeometric term and raises $F(r)$ at intermediate radii, leading to a modest increase of the outer horizon. Finally, the η-panel clearly exhibits the monopole's distinctive role: larger η shifts the entire curve downward at small and intermediate radii, pushing the zero of $F(r)$ to larger r and thereby enlarging the horizon radius. This graphical behavior confirms that the global monopole chiefly governs the size of the outer horizon through a deficit-angle effect, while the Murnaghan parameters dictate how the nonlinear fluid backreaction alters the slope and curvature of the metric function near the horizon.

To probe the fundamental geometric properties of the BH solution, we analyze its curvature invariants, specifically, the Ricci scalar $\mathcal{R}$, the squared Ricci $\mathcal{R}_{\mu\nu}\mathcal{R}^{\mu\nu}$ and the Kretschmann scalar $\mathcal{R}_{\alpha\beta\mu\nu}\mathcal{R}^{\alpha\beta\mu\nu}$. These quantities offer a coordinate independent means of diagnosing singular

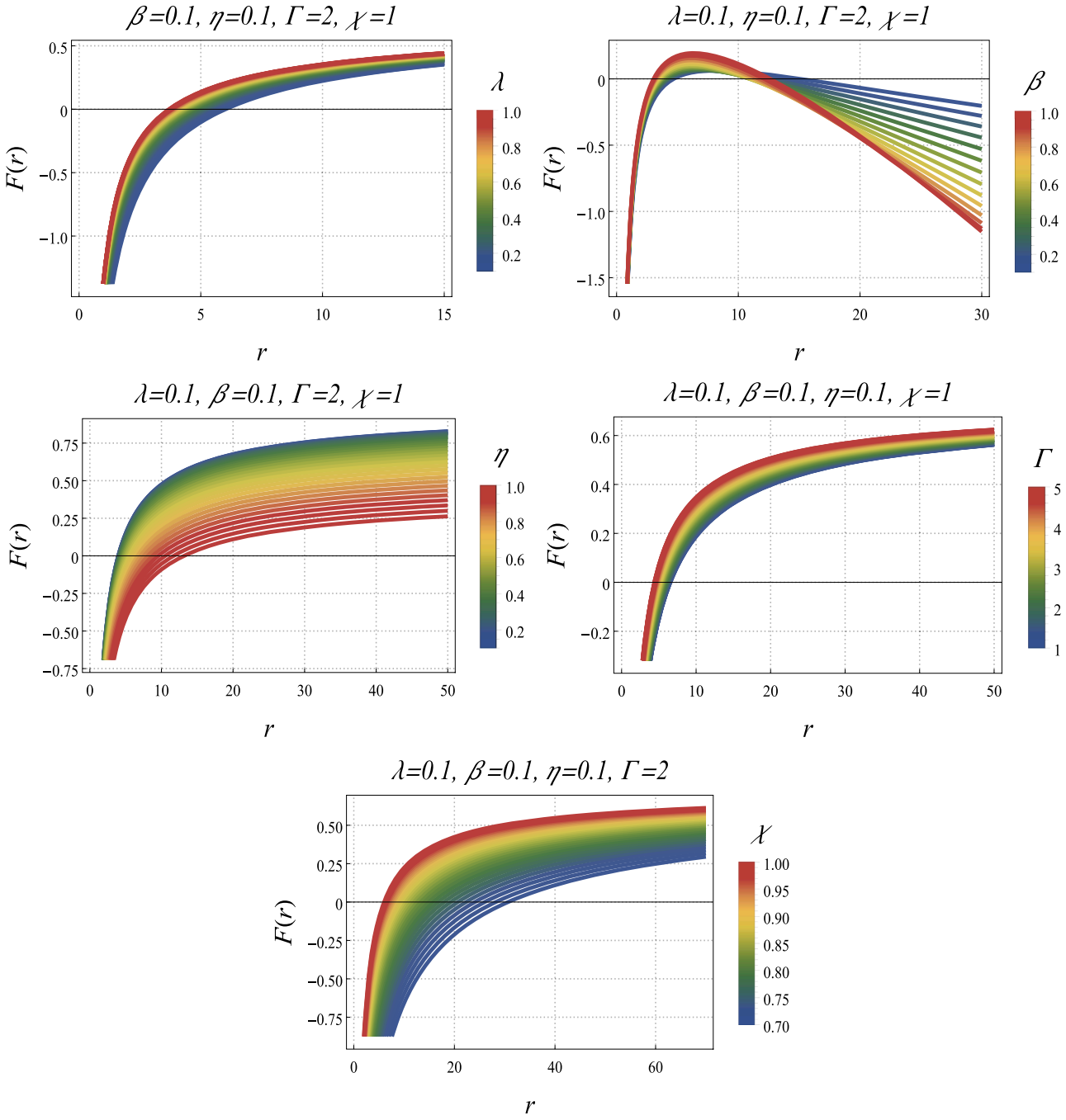

Fig. 4. The metric function $F(r)$ plots against r for various values of the Murnaghan parameters $(\lambda, \beta, \chi, \Gamma)$ and the global monopole parameter η with $M = 1$.

behavior and verifying the uniqueness and regularity of the spacetime. Both invariants are derived from the metric function (27) and encapsulate the gravitational response of the system to the matter content and geometry, providing critical insight into the physical viability of the solution. Thus, the two scalars are given, respectively by

$$R = \frac{\left(\frac{1-\beta}{\lambda}\right)^{\Gamma}\left(4\lambda r^{\frac{3\beta}{\Gamma}} + (3\beta+1)\chi^2 r^{3/\Gamma}\right)\left(\frac{\chi^2 r^{\frac{3-3\beta}{\Gamma}}}{\lambda}+1\right)^{-\Gamma}}{\lambda r^{\frac{3\beta}{\Gamma}} + \chi^2 r^{3/\Gamma}} + \frac{16\pi\eta^2}{r^2}, \tag{28}$$

$$\mathcal{R}_{\mu\nu}\mathcal{R}^{\mu\nu} = \frac{\left(\frac{1-\beta}{\lambda}\right)^{2\Gamma}\left(\left(9\beta^2-6\beta+5\right)\chi^4 r^{6/\Gamma} + 8\lambda^2 r^{\frac{6\beta}{\Gamma}} + 4(3\beta+1)\lambda\chi^2 r^{\frac{3(\beta+1)}{\Gamma}}\right)\left(\frac{\chi^2 r^{\frac{3-3\beta}{\Gamma}}}{\lambda}+1\right)^{-2\Gamma}}{2\left(\lambda r^{\frac{3\beta}{\Gamma}} + \chi^2 r^{3/\Gamma}\right)^2}$$
$$+ \frac{32\pi\eta^2\left(\frac{1-\beta}{\lambda}\right)^{\Gamma}\left(\frac{\chi^2 r^{\frac{3-3\beta}{\Gamma}}}{\lambda}+1\right)^{-\Gamma}}{r^2} + \frac{128\pi^2\eta^4}{r^4}, \tag{29}$$

$$\mathcal{R}_{\alpha\beta\mu\nu}\mathcal{R}^{\alpha\beta\mu\nu} = \frac{1}{9\lambda^2 r^6}\left\{4\lambda^2\left(r^3\left(\frac{1-\beta}{\lambda}\right)^{\Gamma}{}_2F_1\left(\Gamma, \frac{\Gamma}{1-\beta}; \frac{\Gamma}{1-\beta}+1; -\frac{r^{\frac{3-3\beta}{\Gamma}}\chi^2}{\lambda}\right) + 6\left(M + 4\pi\eta^2 r\right)\right)^2\right.$$
$$+ \frac{1}{\left(\lambda r^{\frac{3\beta}{\Gamma}} + \chi^2 r^{3/\Gamma}\right)^2}\left(r^{-\frac{6\beta}{\Gamma}}\left(\frac{\chi^2 r^{\frac{3-3\beta}{\Gamma}}}{\lambda}+1\right)^{-2\Gamma}\left(2r^3\left(\frac{1-\beta}{\lambda}\right)^{\Gamma}\left(\lambda r^{\frac{3\beta}{\Gamma}} + \chi^2 r^{3/\Gamma}\right)^2\right.\right.$$
$$\times{}_2F_1\left(1, 1-\frac{\beta\Gamma}{\beta-1}; \frac{\Gamma}{1-\beta}+1; -\frac{r^{\frac{3-3\beta}{\Gamma}}\chi^2}{\lambda}\right) + 3\lambda r^{\frac{3\beta}{\Gamma}}\left(4M\left(\lambda r^{\frac{3\beta}{\Gamma}} + \chi^2 r^{3/\Gamma}\right)\left(\frac{\chi^2 r^{\frac{3-3\beta}{\Gamma}}}{\lambda}+1\right)^{\Gamma}\right.$$
$$\left.\left.\left. + 3(\beta-1)\chi^2 r^{\frac{3}{\Gamma}+3}\left(\frac{1-\beta}{\lambda}\right)^{\Gamma}\right)\right)^2 + 4\left(\frac{\chi^2 r^{\frac{3-3\beta}{\Gamma}}}{\lambda}+1\right)^{-2\Gamma}\left(\lambda\left(\frac{\chi^2 r^{\frac{3-3\beta}{\Gamma}}}{\lambda}+1\right)^{\Gamma}\left(r^3\left(\frac{1-\beta}{\lambda}\right)^{\Gamma}\right.\right.\right.$$
$$\left.\left.\left.\times{}_2F_1\left(\Gamma, \frac{\Gamma}{1-\beta}; \frac{\Gamma}{1-\beta}+1; -\frac{r^{\frac{3-3\beta}{\Gamma}}\chi^2}{\lambda}\right) + 6M\right) - 3\lambda r^3\left(\frac{1-\beta}{\lambda}\right)^{\Gamma}\right)^2\right\}. \tag{30}$$

A more detailed examination of the Eqs. (28)–(30) reveals the following observations:

- Near $r \to 0$ the global monopole term dominates and $\mathcal{R} \sim 16\pi\eta^2/r^2$ (divergence $1/r^2$ unless $\eta = 0$); for $r \to \infty$ the Murnaghan contribution decays typically like $r^{-(3-3\beta)}$ for $\beta < 1$, so the far field leading term is set by the competition between this decay and the monopole tail $\propto r^{-2}$ (hence if $\beta > 1/3$ the Murnaghan tail can dominate asymptotically). Parameter limits simplify the structure: $\chi \to 0$ yields an essentially constant Murnaghan element $\sim 4\big((1-\beta)/\lambda\big)^{\Gamma}$, $\beta \to 1$ shrinks the Murnaghan amplitude, and larger Γ slows radial variation.
- Near $r \to 0$ higher powers of η appear and the dominant behaviour is generically $\mathcal{R}_{\mu\nu}\mathcal{R}^{\mu\nu} \propto 128\pi^2\eta^4/r^4$ (unless mass-dependent terms with stronger $1/r$ powers intervene), signalling a more severe singularity than for $\mathcal{R}$; asymptotically the Murnaghan term falls off faster than the monopole tail and the balance again depends on β, so β controls whether fluid or monopole contribution dominate the curvature concentration at large radii.
- The Kretschmann invariant displays the strongest central divergence in general, with a Schwarzschild-like leading piece $\sim \text{const} \cdot M^2/r^6$ coming from the squared mass term in the numerator; if $M = 0$ the most severe divergence reduces and monopole-dependent terms (e.g. $\sim \eta^4/r^4$) dominate instead, while for $r \to \infty$ the invariant decays rapidly (high negative powers of r) with only mild modifications from the hypergeometric/Murnaghan structure, hence the Kretschmann invariant is the most robust diagnostic of a true curvature singularity and confirms that removing η or fine-tuning parameters is necessary to soften or remove the central divergence.

4. Sparsity of Hawking radiation

In this section, we aim to study the sparsity of Hawking radiation in the essence of our BH solution. Essentially, a BH can act similarly to a black body, emitting particles at a temperature close to the surface gravity. Even so, the Hawking radiation flux is quite dissimilar to conventional blackbody radiation in that it emerges rather sparsely throughout the evaporation process. Sparsity $\tilde{\eta}$ measures how frequently a BH emits quanta compared with the natural time-scale set by the quanta's energy: large $\tilde{\eta} \gg 1$ means emissions are rare, well separated in time, and the evaporation proceeds as a sequence of discrete, widely spaced quanta rather than a steady classical flux; conversely $\tilde{\eta} \ll 1$ corresponds to an almost continuous (blackbody-like) emission. In practice $\tilde{\eta}$ compares the square of the thermal wavelength $\lambda_t \sim 1/T_h$ to the effective emitting area $\mathcal{A}_{\text{eff}}$, so sparsity is fundamentally a competition between the quantum wavelength of emitted particles and the geometric size of the emitter. It can therefore be defined as follows [132–134]

$$\tilde{\eta} = \frac{\mathcal{C}}{\tilde{g}}\left(\frac{\lambda_t^2}{\mathcal{A}_{eff}}\right), \tag{31}$$

where $\mathcal{C}$ is a dimensionless constant, $\tilde{g}$ is the degeneracy factor of the spin of the emitted quanta, $\lambda_t = 2\pi/T_H$ denotes the thermal wavelength, and $\mathcal{A}_{eff} = 27\mathcal{A}_{BH}/4$ is the related effective area of the BH. In the ordinary case of a Schwarzschild BH and the emission of massless spin-1 bosons, we have $\lambda_t = 8\pi r_h^2 \implies \tilde{\eta}_{Sch} = 64\pi^3/27 \approx 73.49$. By way of comparison, look at $\eta \ll 1$ for blackbody radiation.

It turns out to be advantageous, at first glance, to implement the so-called surface gravity to determine the corresponding temperature, which is expressed as follows

$$\kappa = \left(-\frac{1}{2}\nabla_\mu\chi_\nu\nabla^\mu\chi^\nu\right)^{1/2}\Big|_{r=r_h} = \frac{1}{2}F'(r)\Big|_{r=r_h} \tag{32}$$

where $\chi^\mu = \partial/\partial t$ is a Killing vector. Thus, to derive the pertinent surface gravity, it is convenient to look at the metric function (27) and use the mass term which is given by

$$M = \frac{1}{6}r_h\left(24\pi\eta^2 + r_h^2\left(\frac{1-\beta}{\lambda}\right)^{\Gamma}{}_2F_1\left(\Gamma, \frac{\Gamma}{1-\beta}; \frac{\Gamma}{1-\beta}+1; -\frac{r_h^{\frac{3-3\beta}{\Gamma}}\chi^2}{\lambda}\right) - 3\right) \tag{33}$$

into Eq. (32). So the surface gravity related to the BH solution can be accurately stated as follows:

$$\kappa = \frac{24\pi\eta^2 + 2r_h^2\left(\frac{1-\beta}{\lambda}\right)^{\Gamma}{}_2F_1\left(\Gamma, \frac{\Gamma}{1-\beta}; \frac{\Gamma}{1-\beta}+1; -\frac{r_h^{\frac{3-3\beta}{\Gamma}}\chi^2}{\lambda}\right) - 3r_h^2\left(\frac{1-\beta}{\lambda}\right)^{\Gamma}\left(\frac{\chi^2 r_h^{\frac{3-3\beta}{\Gamma}}}{\lambda}+1\right)^{-\Gamma} - 3}{6r_h}. \tag{34}$$

To find the corresponding Hawking temperature, we follow the formula $T = \kappa/2\pi$, which yields the temperature in such a way as

$$T_h = \frac{24\pi\eta^2 + 2r_h^2\left(\frac{1-\beta}{\lambda}\right)^{\Gamma}{}_2F_1\left(\Gamma, \frac{\Gamma}{1-\beta}; \frac{\Gamma}{1-\beta}+1; -\frac{r_h^{\frac{3-3\beta}{\Gamma}}\chi^2}{\lambda}\right) - 3r_h^2\left(\frac{1-\beta}{\lambda}\right)^{\Gamma}\left(\frac{\chi^2 r_h^{\frac{3-3\beta}{\Gamma}}}{\lambda}+1\right)^{-\Gamma} - 3}{12\pi r_h}. \tag{35}$$

In accordance with the first law of BH thermodynamics, entropy is calculated as follows

$$S = T^{-1}\int \frac{\partial M}{\partial r_h}\,\mathrm{d}r_h = \pi r_h^2. \tag{36}$$

To highlight the real nature of the physical phenomenon of sparsity in BHs surrounded by a polytropic structure, we consider the relevant Hawking temperature (35) and, in accordance with the definition of sparsity (31), we obtain

$$\tilde{\eta} = \frac{64\pi^3}{3\,N(r_h)^2} = \frac{4\pi}{27\,r_h^2T_h^2}, \qquad T_h = \frac{N(r_h)}{12\pi r_h} \tag{37}$$

with

$$N(r_h) \equiv 24\pi\eta^2 - 3 + r_h^2\left(\frac{1-\beta}{\lambda}\right)^{\Gamma}\left(2\,{}_2F_1\left(\Gamma, \frac{\Gamma}{1-\beta}; \frac{\Gamma}{1-\beta}+1; -\frac{\chi^2 r_h^{\frac{3(1-\beta)}{\Gamma}}}{\lambda}\right) - 3\left(1+\frac{\chi^2 r_h^{\frac{3(1-\beta)}{\Gamma}}}{\lambda}\right)^{-\Gamma}\right). \tag{38}$$

To better understand how sparsity could be physically modelled under the variations of the Murnaghan gas and the global monopole parameters, it is important to examine the appropriate behaviour in the limit as the horizon approaches zero $r_h \to 0$. It is evident that the term accompanying the r_h^2 terms must vanish as r_h approaches zero, and thus

$$N \simeq 24\pi\eta^2 - 3, \quad \Rightarrow \quad \tilde{\eta} \simeq \frac{64\pi^3}{3(24\pi\eta^2-3)^2}, \tag{39}$$

indicating that $\tilde{\eta}$ is finite near $r_h = 0$ except when $24\pi\eta^2 - 3 = 0$. Physical consistency requires $T_h > 0 \Rightarrow N(r_h) > 0$; in the $r_h \to 0$ approximation this gives $\eta^2 > 3/(24\pi) = 1/(8\pi)$.

On the other hand, at large horizon limit $r_h \to \infty$ with the typical physical case such that $(\beta < 1)$, one has

$$N(r_h) \sim 3\left(\frac{1-\beta}{\lambda}\right)^{2\Gamma} r_h^{3\beta-1} + 24\pi\eta^2 - 3. \tag{40}$$

This yields three regimes determined by the sign of $3\beta - 1$:

- If $\beta > 1/3$ then $3\beta - 1 > 0$, $N \propto r_h^{3\beta-1}$ grows with r_h and
$$\tilde{\eta} \sim r_h^{-2(3\beta-1)} = r_h^{2-6\beta} \quad (\beta > 1/3). \tag{41}$$
Hence sparsity decreases with r_h (emission becomes relatively less sparse as the BH grows, due to the Murnaghan-driven temperature growth).
- If $\beta = 1/3$ then N acts like a constant at large r_h, so $\tilde{\eta}$ tends to a constant (Schwarzschild-like behaviour).
- If $\beta < 1/3$ then $3\beta - 1 < 0$, the r_h-dependent terms decay and the constant $24\pi\eta^2 - 3$ dominates; $\tilde{\eta}$ asymptotes to a constant set by that value.

Inspecting monotonicity and extremality is essential for a more concrete examination of the profound physical behaviour of the present

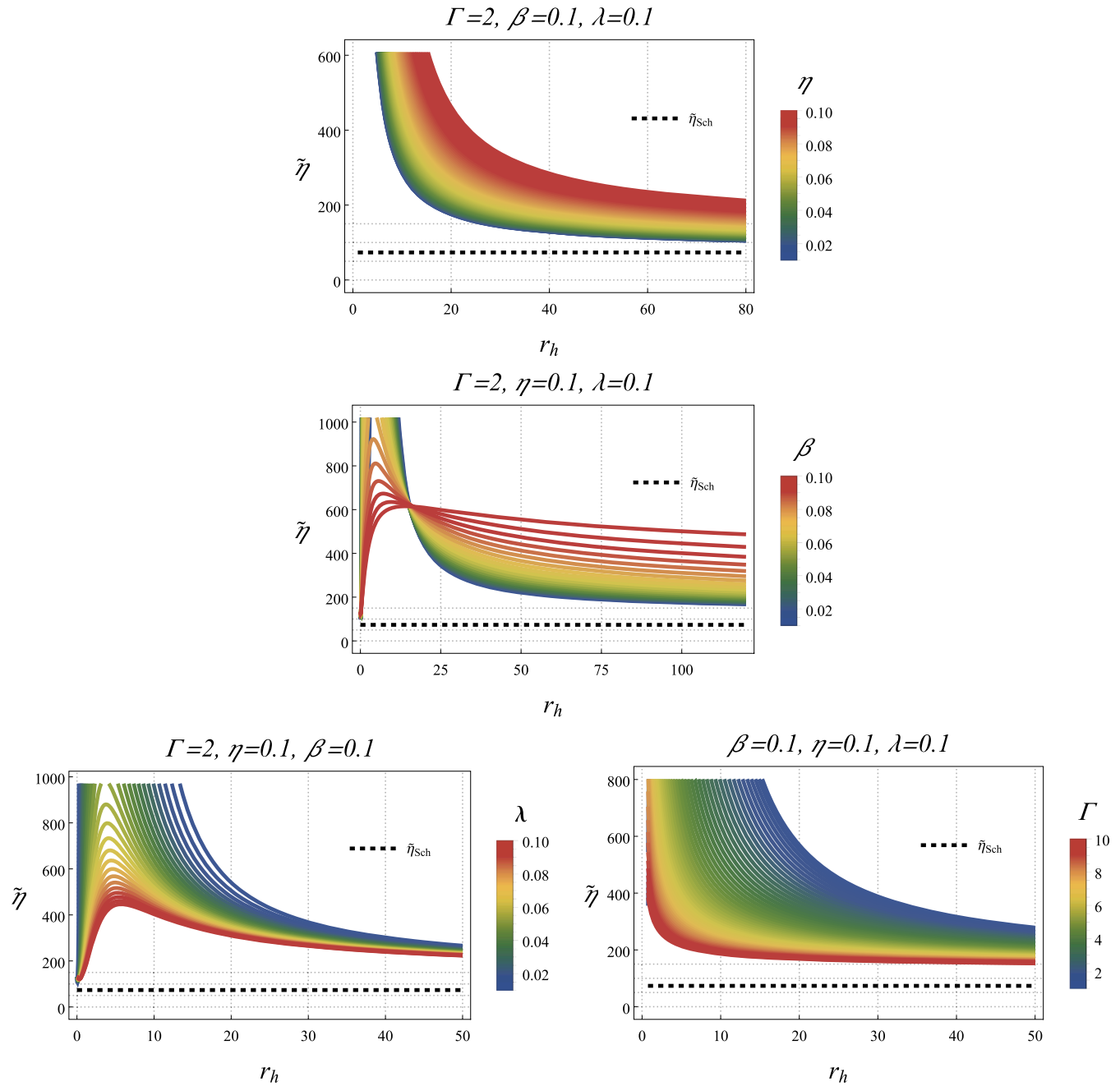

Fig. 5. Sparsity of Hawking radiation $\tilde{\eta}$ as a function of the event-horizon radius r_h for representative values of the model parameters. The dashed reference curve shows the Schwarzschild value $\tilde{\eta}_{\rm Sch} = 73.49$.

process. Consequently, differentiating the sparsity of Hawking radiation yields the following expression

$$\frac{d\widetilde{\eta}}{dr_h} = -\frac{128\pi^3}{3}\frac{N'(r_h)}{N(r_h)^3}, \tag{42}$$

in which the sign of $N'(r_h)$ controls whether $\widetilde{\eta}$ increases or decreases with r_h. In addition, the roots of $N(r_h)$ (i.e. $T_h = 0$) are extremal points where $\widetilde{\eta} \to \infty$ - these mark thermodynamically special configurations and must be treated carefully.

Role of the monopole η and physical interpretation: the additive term $24\pi\eta^2$ raises N (and thus T_h) for given r_h, so, other things equal, a larger monopole parameter tends to lower $\widetilde{\eta}$ (reduce sparsity). However, the full effect depends on competition with Murnaghan terms (hypergeometric terms) which can either increase or decrease N depending on $\beta, \lambda, \chi, \Gamma$. Physically, $\widetilde{\eta}$ is controlled solely by the combination $r_h T_h$: hotter holes (larger T_h) are less sparse, and larger geometric area (larger r_h) tends to increase sparsity unless T_h grows fast enough to compensate (the $\beta > 1/3$ case).

The sparsity parameter $\tilde{\eta}$ vs horizon radius r_h is plotted in Fig. 5 with the Schwarzschild reference (dashed) $\tilde{\eta}_{\rm Sch} = 64\pi^3/27 \simeq 73.49$. Graphically speaking, Increasing η results in a downward vertical shift of the curves at small and moderate r_h, bringing them closer to or below the dashed Schwarzschild line. This phenomenon suggests a less sparse (more continuous) emission. Increasing β also steepens the falloff of $\tilde{\eta}(r_h)$; for $\beta \gtrsim 1/3$, the curves decline more rapidly and often intersect below the Schwarzschild reference at moderate radii. In addition, a larger value of λ compresses the family of curves towards the dashed line, resulting in a smaller vertical spread. Conversely, a smaller λ causes the curves to fan outwards, leading to the most significant departures from Schwarzschild. On the other hand, increasing Γ leads to a slight

downward shift at intermediate values of r_h, followed by saturation. The curves corresponding to higher values of Γ are positioned slightly lower but tend to converge at larger radii. Lastly, a larger value of χ amplifies the vertical deviations from the dashed curve, while a smaller value of χ causes the family to converge towards the Schwarzschild reference.

Broadly speaking, curves situated below the dashed line represent relatively more continuous (blackbody-like) emission, while those above indicate comparatively sparser emission. Observationally, the parameters η and χ influence vertical shifts, β affects slope and steepness, and λ and Γ govern clustering towards the Schwarzschild solution.

Regions of parameter space for which the sparsity parameter satisfies $\tilde{\eta} < \tilde{\eta}_{\rm Sch}$ correspond to a regime in which the BH's quantum emission is relatively more "continuous" (less temporally sparse) compared with a Schwarzschild hole of the same horizon radius. Operationally this arises because the dimensionless combination $r_h T_h$ increases (or decreases less rapidly) for those parameter choices, so the mean time between quanta shortens compared with the Schwarzschild reference (see Eq. (37) and Fig. 5). Observationally while direct detection of Hawking quanta from astrophysical stellar-mass or supermassive holes remains infeasible-the most promising arenas to exploit this behaviour are primordial / low-mass BHs, where the absolute emission rate and spectral intensity are larger, and indirect signatures in high-energy diffuse backgrounds (for example, gamma-ray fluxes) or in transient bursts expected during the final evaporation stages. A less sparse emission (lower $\tilde{\eta}$) amplifies the high-frequency tail of the emitted spectrum and increases the instantaneous flux, which would (in principle) increase the detectability of bursts from evaporating microholes or tighten constraints on low-mass PBH abundance. In addition, combined modelling of greybody spectra (Section 6) and QNM-inferred horizon redshifts could help distinguish whether a measured enhancement in radiative flux arises from a local stiffening of the fluid (Murnaghan sector) or from a global redshift effect (monopole).

5. Quasinormal modes

In this section, we study the QNMs of the BH solution. QNMs quantify the responses of BHs to perturbations induced by test fields. We first study the variations of the QNMs corresponding to the scalar and the electromagnetic of the BH solution (Murnaghan and global monopole) with the model parameters in the frequency domain using the 3$^{\rm th}$-order Padé-averaged Wentzel-Kramers-Brillouin (WKB) method. In this work, we start with a brief introduction to the Padé-averaged WKB method.

5.1. The Padé-averaged WKB method for QNMs

Mashhoon [98] was the first to introduce a semi-analytic WKB formula, formulating it by approximating the effective potential with the inverse Pöschl-Teller potential. This approach was subsequently generalised by Schutz and Will [99] through the application of the WKB approximation. In this method, the effective potential is matched at the asymptotic regions, specifically near the event horizon and at infinity-by employing a Taylor series expansion. Building on this foundation, Iyer and Will [100] expanded the accuracy of the formula to third order, resulting in markedly more precise fundamental mode calculations, with errors reduced to fractions of a percent. Even with advancements extending to the sixth order [101], the WKB formula maintains high accuracy primarily in the regime where $\ell \gg n$, with ℓ and n representing the multipole and overtone indices, respectively. In more complex settings, particularly those involving non-Schwarzschild metrics, this method becomes less reliable for extracting additional modes. The accuracy diminishes notably for cases where $n \geq \ell$, reflecting the fact that the WKB approach does not guarantee improved convergence at successive orders; that is, higher order does not always equate to higher accuracy. The use of Padé approximants serves to better analyse the large-order behaviour of the WKB expansion. Given the requirement for highly precise estimates of QNMs, we utilise the Padé-averaged WKB technique, as outlined in Refs[102,103]. This method allows us to compute the frequency-domain QNMs of the BH solution when subjected to scalar and electromagnetic perturbations. An outline of this enhanced WKB approach follows.

For a wave-type equation

$$\frac{d^2\Psi}{dx^2} = U(x,\omega)\Psi, \tag{43}$$

the WKB approximation gives asymptotic solutions expressed as a superposition of ingoing and outgoing waves [104]. These solutions are matched at the extrema of the effective potential using a Taylor expansion. The method yields a closed-form expression for the QNM frequencies as [103]

$$\begin{aligned}\omega^2 =& V_0 + A_2(\mathcal{K}^2) + A_4(\mathcal{K}^2) + A_6(\mathcal{K}^2) + \ldots - i\mathcal{K}\sqrt{-2V_2}\big(1 + A_3(\mathcal{K}^2)\\ &+A_5(\mathcal{K}^2) + A_7(\mathcal{K}^2) + \ldots\big),\end{aligned} \tag{44}$$

To control the divergence of the Taylor series, Padé approximants are employed [102]. These are based on a polynomial $P_k(\epsilon)$, constructed in powers of an auxiliary order parameter ϵ, modifying Eq. (44) as

$$\begin{aligned}P_k(\epsilon) =& V_0 + A_2(\mathcal{K}^2)\epsilon^2 + A_4(\mathcal{K}^2)\epsilon^4 + A_6(\mathcal{K}^2)\epsilon^6 + \ldots\\ &- i\mathcal{K}\sqrt{-2V_2}\big(\epsilon + A_3(\mathcal{K}^2)\epsilon^3 + A_5(\mathcal{K}^2)\epsilon^5 + \ldots\big)\end{aligned} \tag{45}$$

The Padé approximant $P_{\tilde{n}/\tilde{m}}(\epsilon)$ corresponding to the polynomial $P_k(\epsilon)$ is expressed as a rational function [102,103]:

$$P_{\tilde{n}/\tilde{m}}(\epsilon) = \frac{Q_0 + Q_1\epsilon + \ldots + Q_{\tilde{n}}\epsilon^{\tilde{n}}}{R_0 + R_1\epsilon + \ldots + R_{\tilde{m}}\epsilon^{\tilde{m}}}, \tag{46}$$

where $\tilde{n} + \tilde{m} = k$. To assess the precision of the method, we compute the associated error in the frequency values. Since each order contributes corrections to both the real and imaginary parts of ω^2, the uncertainty in ω_k at order k is estimated by

$$\Delta_k = \frac{\omega_{k+1} - \omega_{k-1}}{2} \tag{47}$$

5.2. Massless scalar perturbations

We consider massless scalar perturbations and start with the Klein-Gordon equation. The perturbed metric can be recast as follows [105, 106]:

$$ds^2 = -g_{tt}|dt^2 + g_{rr}dr^2 + r^2d\theta^2 + r^2\sin^2\theta\big(d\phi - q_1dt - q_2dr - q_3d\theta\big)^2 \tag{48}$$

Here, q_1, q_2, and q_3 are functions of t, r, and θ (but are independent of ϕ). They appear in the field equations in specific combinations, are first order in smallness, and play a key role in governing odd-parity perturbations. In the static case, q_2 and q_3 are taken to vanish [105]. We employ the tetrad formalism and work with a basis e^{μ}_{a} associated with the metric $g_{\mu\nu}$, which satisfies

$$\begin{aligned}&e^{(a)}_{\mu}e^{\mu}_{(b)} = \delta^{(a)}_{(b)}\\ &e^{(a)}_{\mu}e^{\nu}_{(a)} = \delta^{\nu}_{\mu}\\ &e^{(a)}_{\mu} = g_{\mu\nu}\eta^{(a)(b)}e^{\nu}_{(b)}\\ &g_{\mu\nu} = \eta_{(a)(b)}e^{(a)}_{\mu}e^{(b)}_{\nu} = e_{(a)\mu}e^{(a)}_{\nu}.\end{aligned} \tag{49}$$

In the new basis, vector and tensor quantities are projected as

$$\begin{aligned}&P_{\mu} = e^{(a)}_{\mu}P_{(a)},\\ &P_{(a)} = e^{\mu}_{(a)}P_{\mu},\\ &A_{\mu\nu} = e^{(a)}_{\mu}e^{(b)}_{\nu}A_{(a)(b)},\\ &A_{(a)(b)} = e^{\mu}_{(a)}e^{\nu}_{(b)}A_{\mu\nu}.\end{aligned} \tag{50}$$

Considering the propagation of a massless scalar field around the BH, and assuming that the backreaction of the scalar field on the spacetime is

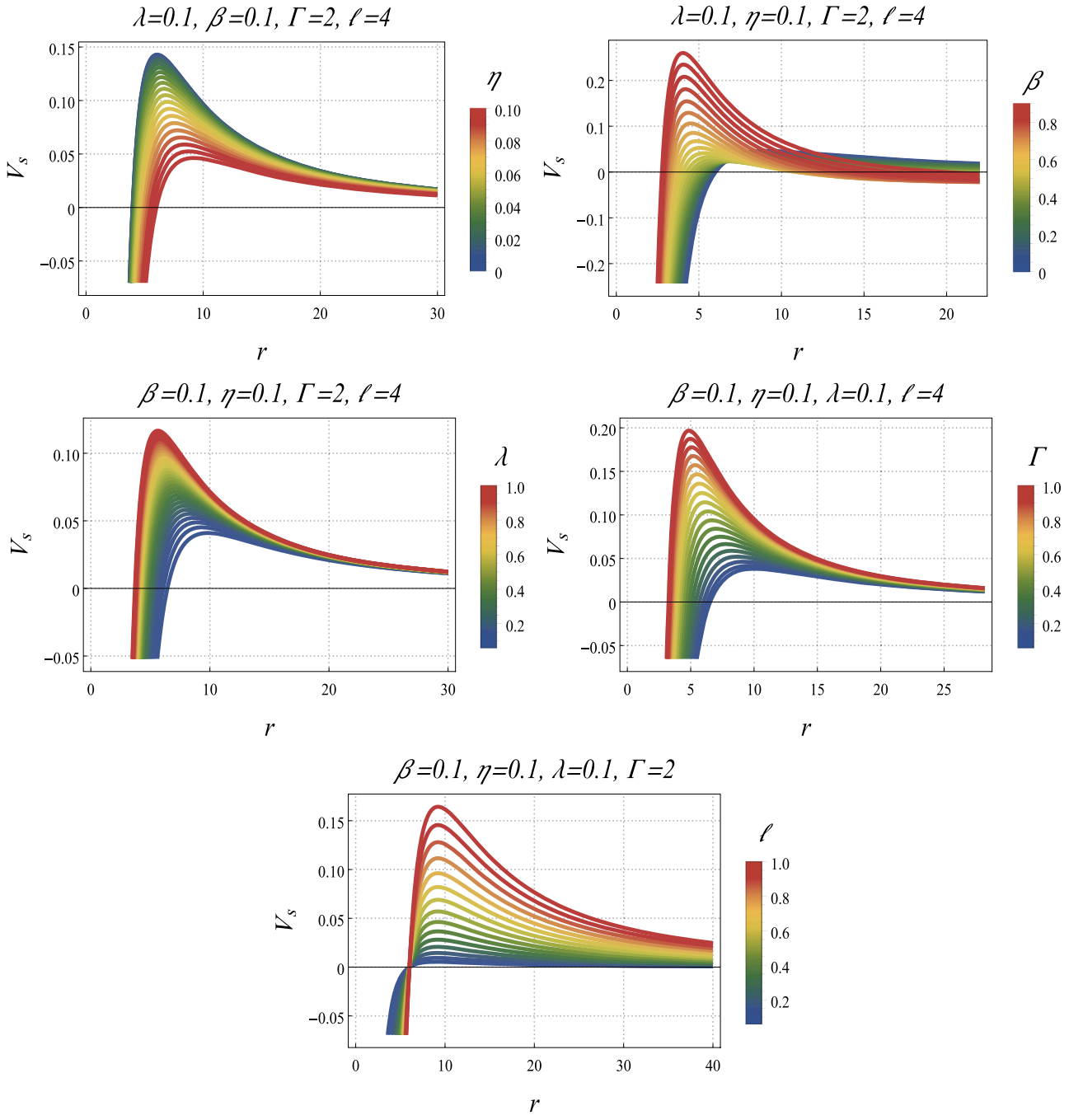

Fig. 6. Scalar potential $V_s(r)$ as a function of the radial coordinate r for representative values of the model parameters and for several multipole numbers ℓ with $M = 1$.

negligible, the scalar QNMs are governed by the Klein-Gordon equation, given by

$$\Box\Phi = \frac{1}{\sqrt{-g}}\partial_\mu(\sqrt{-g}g^{\mu\nu}\partial_\nu\Phi) = 0. \tag{51}$$

We neglect the back-reaction of the field and consider Eq. (48) only up to the zeroth order:

$$ds^2 = -|g_{tt}|dt^2 + g_{rr}dr^2 + r^2 d\Omega_2^2 \tag{52}$$

The scalar field can be decomposed using spherical harmonics as

$$\Phi(t, r, \theta, \phi) = \frac{1}{r}\sum_{\ell,m}\psi_\ell(t, r)Y_{\ell m}(\theta, \phi), \tag{53}$$

where $\psi_l(t, r)$ is the time-dependent radial wave function and ℓ and m are indices of the spherical harmonics Y_{lm}. Then, Eq. (51) yields

$$\partial^2_{r_*}\psi(r_*)_l + \omega^2\psi(r_*)_l = V_s(r)\psi(r_*)_l, \tag{54}$$

where r_* is the tortoise coordinate defined as

$$\frac{dr_*}{dr} = \sqrt{g_{rr}\,|g_{tt}^{-1}|} \tag{55}$$

and $V_s(r)$ is the effective potential of the field given by

$$V_s(r) = |g_{tt}|\left(\frac{\ell(\ell+1)}{r^2} + \frac{1}{r\sqrt{|g_{tt}|g_{rr}}}\frac{d}{dr}\sqrt{|g_{tt}|g_{rr}^{-1}}\right). \tag{56}$$

which vanishes at the event horizon (since $|g_{tt}| \to 0$) and decays to zero at large r in the asymptotic region. Hence $V_s(r)$ generically forms a sin-

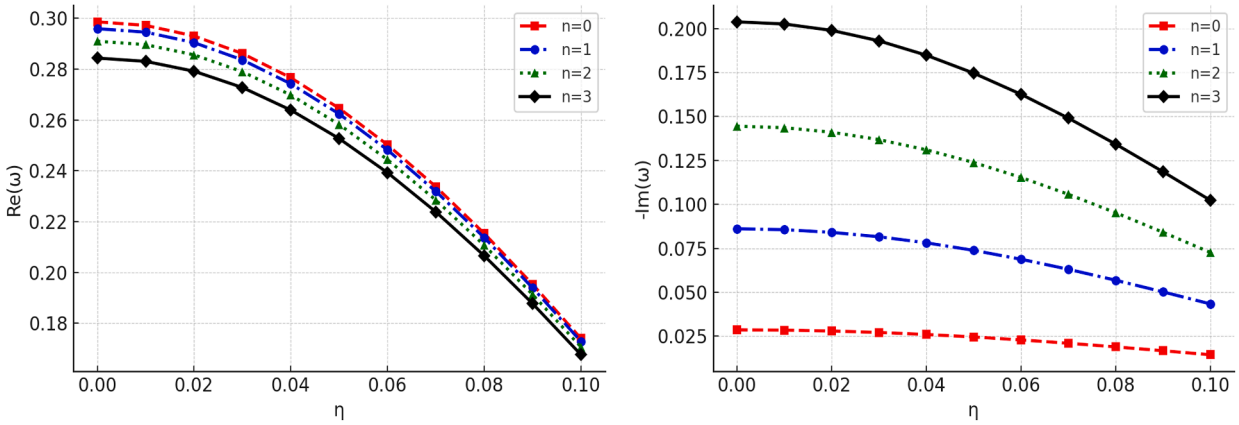

Fig. 7. Variation of the scalar QNMs with respect to the phantom global monopole parameter with $\Gamma =, \beta = 0.1, \lambda = 0.1, \chi = 1, M = 1$ and $\ell = 4$.

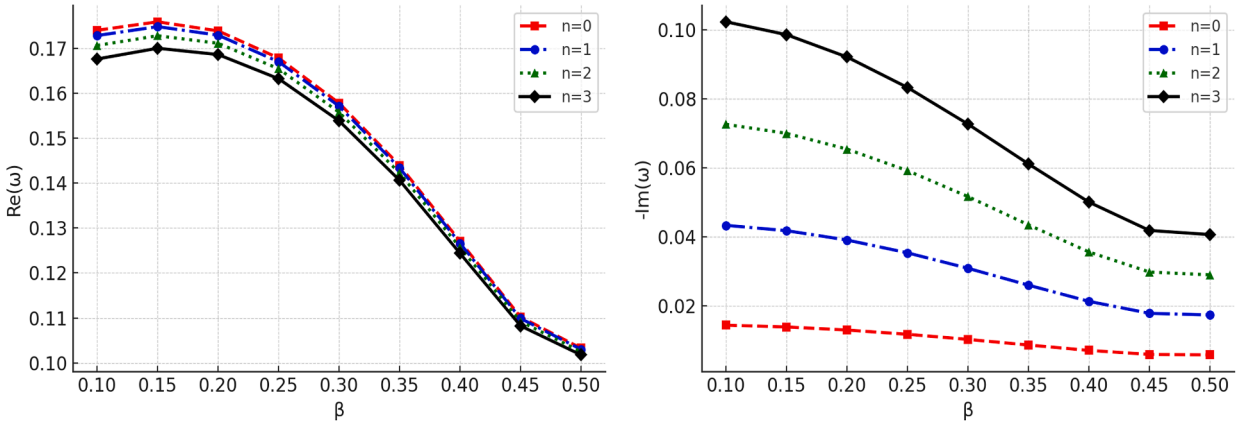

Fig. 8. Variation of the scalar QNMs with respect to β with $\Gamma = 2, \eta = 0.01, \lambda = 0.1, \chi = 1, M = 1$ and $\ell = 4$.

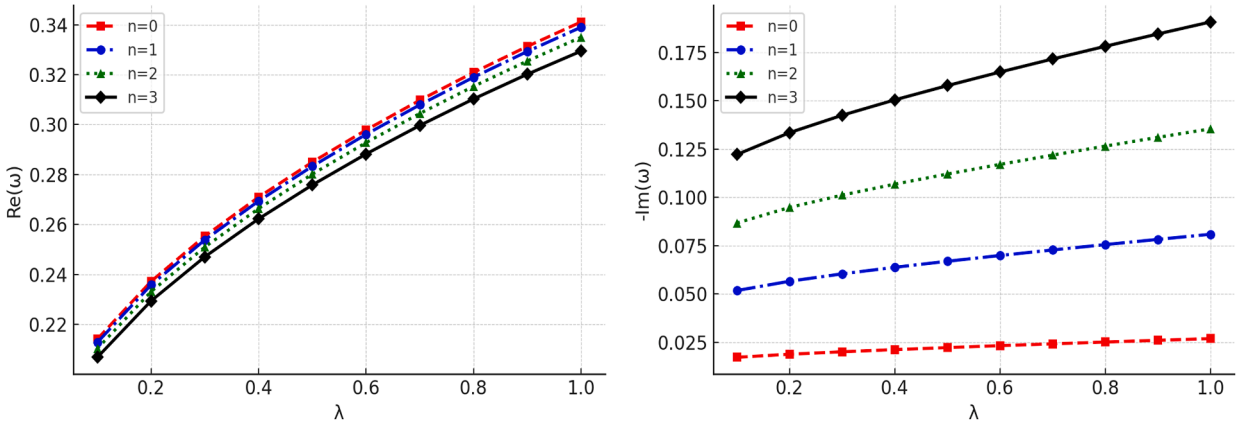

Fig. 9. Variation of the scalar QNMs with respect to λ with $\Gamma = 2, \eta = 0.01, \beta = 0.1, \chi = 1, M = 1$ and $\ell = 4$.

gle barrier outside the horizon (the photon-sphere region) whose peak position r_{peak} and height $V_{\max}$ control the dominant QNM real part (oscillation frequency) and the barrier transmission (damping). Because the second term contains radial derivatives of the metric functions, the precise shape of the barrier is sensitive to both the redshift factor $|g_{tt}|$ and to the radial profile $F'(r)$, $F''(r)$ of the background geometry; these analytic features underlie the plotted potentials and justify the use of the WKB/Padé method.

Moreover, the scalar effective potential $V_s(r)$ obtained from the standard perturbation reduction contains not only the centrifugal term $\propto \ell(\ell+1)/r^2$ multiplied by the redshift $F(r)$, but also contributions proportional to the first and second derivatives $F'(r)$ and $F''(r)$. Because the metric function (27) contains a ${}_2F_1$ contribution sourced by the Murnaghan density, differentiation introduces explicit dependence on the Murnaghan parameters $\{\beta, \Gamma, \lambda, \chi\}$ through derivatives of the hypergeometric argument and its coefficients. Concretely, schematically one may write the Regge-Wheeler–type form

$$V_s(r) = F(r)\left[\frac{\ell(\ell+1)}{r^2} + \frac{1}{r}F'(r) + \frac{1}{2}F''(r)\right] + \cdots,$$

so any parameter that alters F' or F'' (i.e. the Murnaghan sector) directly reshapes the barrier height and width, producing the derivative-sensitive responses observed in Fig. 6 and Tables 1–3. This structural dependence makes the scalar channel a direct probe of local fluid stiffness and nonlinearity, whereas channels that lack derivative sensitivity

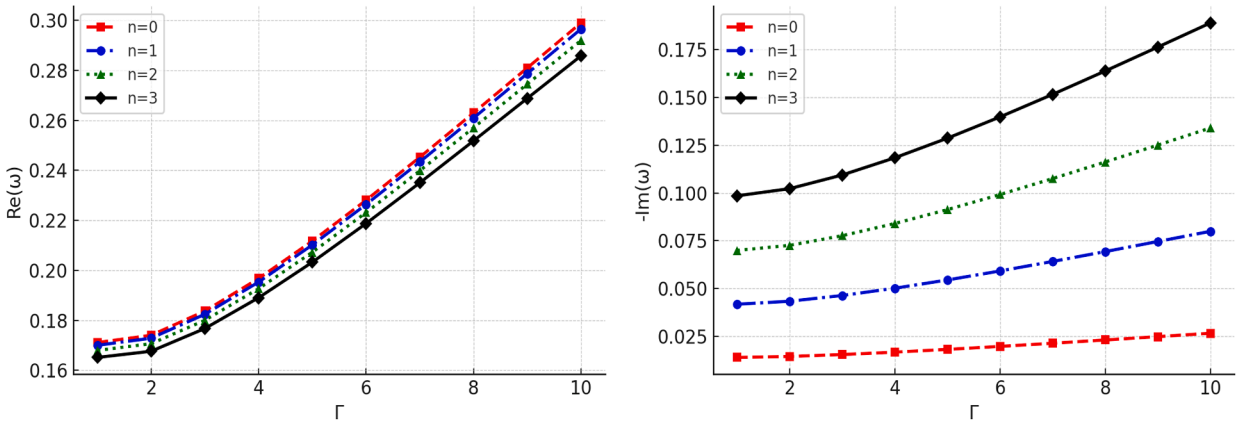

Fig. 10. Variation of the scalar QNMs with respect to Γ with $\beta = 0.1, \eta = 0.01, \lambda = 0.1, \chi = 1$, $M = 1$ and $\ell = 4$.

(for example the electromagnetic channel) remain comparatively insensitive.

Graphically (see Fig. 6) and physically, parameters that raise and narrow the scalar barrier (increase $V_{\max}$ and make it steeper) lead to larger Re(ω) and larger |Im(ω)| (faster decay), while parameters that lower or broaden the peak reduce Re(ω) and lengthen the mode lifetime. Concretely in our model: Increasing the nonlinearity amplitude λ or the polytropic index Γ tends to stiffen the Murnaghan contribution and raise the scalar peak; increasing the phantom coupling β typically redistributes the fluid contribution so the peak is lowered and modes live longer; the integration amplitude χ scales the overall nonlinear effect and therefore controls the magnitude of the departure of V_s from the Schwarzschild-like shape. These parameter trends correspond directly to the numerical panels for V_s and to the QNM tables (see Tables 1, 2 and Figs. 7–10) and explain why scalar QNMs show stronger sensitivity to $\lambda, \Gamma, \beta, \chi$ than to the monopole parameter η.

5.3. Numerical and graphical analysis of scalar perturbations and QNM spectra for the spacetime solution $g_{\mu\nu}$ (27) under systematic variation of the paramter set $\{\eta, \lambda, \beta, \Gamma\}$, employing the 3th-order WKB-Padé method

The Padé accuracy method at 3rd-order provides QNM frequencies for the multipole number $\ell = 4$ across various parameter model values and overtones $n = 0, 1, 2, 3$, which helps improve our understanding of the analysis of the scalar perturbation along the spacetime solution (6). For that reason, the primary analysis is devoted to examining the numerical QNM frequencies by means of Tables 1 and 2, then to graphical behaviour through Figs. 7–10.

5.3.1. Tables 1 and 2

Table 1 displays the scalar-mode frequency shifts caused by the global-monopole parameter η. Two clear and robust trends emerge across all overtones shown: (i) the real part Re(ω) decreases monotonically (or weakly monotonically, depending on the detailed sampling) as η increases, indicating that the characteristic oscillation frequency is lowered by the monopole-induced solid-angle deficit; and (ii) the damping |Im(ω)| also decreases with increasing η in the displayed slice, so modes become longer lived for larger monopole strength. These trends persist for the fundamental and for the first few overtones, although higher overtones show a larger relative uncertainty and a faster increase in |Im(ω)| with overtone number n. Importantly, 3th-order WKB-Padé uncertainty column Δ is uniformly smaller than the parameter-induced shifts for the lowest overtones, so the monotonic trends are numerically robust. The monopole term alters the redshift and the effective centrifugal barrier experienced by scalar perturbations. This modification results in a shift of the potential peak and a reduction in the leakage into the horizon. Consequently, this explains the simultaneous decrease in both frequency and damping.

Table 2 quantifies how the Murnaghan sector (β, λ, Γ) controls the scalar QNM spectrum. The dominant features is parameter-specific: increasing the nonlinearity amplitude λ or the shape index Γ generally raises Re(ω) (modes oscillate faster) and increases the damping magnitude |Im(ω)| (modes decay faster), while increasing β (within the sub-phantom range used) tends to lower Re(ω) and can slightly reduce damping. This behaviour is consistent with the Murnaghan parameters changing the height and width of the effective potential: larger λ or Γ stiffen the potential and make it taller/narrower (higher frequency, larger leakage), whereas larger β shifts the radial distribution of the scalar fluid contribution in a way that reduces the potential peak near the photon sphere. Across the displayed parameter ranges, the 3th-order WKB-Padé uncertainty Δ remains small for $n = 0$ and $n = 1$, but grows for higher n; therefore, conclusions for the fundamental and first overtone are robust.

5.3.2. Figs. 7–10

Fig. 7 shows the response of the scalar QNM spectrum to changes in the global monopole parameter η (with other Murnaghan parameters fixed). As η increases, the real part Re(ω) shows a modest monotonic decrease for the fundamental and first overtones, indicating that the effective potential's peak frequency is shifted downward by the solid-angle deficit induced by the monopole core. The damping (−Im(ω), plotted as positive values) also decreases slightly with η, signalling a slower decay (longer-lived modes) for larger monopole charge. This mirrors the electromagnetic response in Fig. 12 but with a systematically smaller change in damping for scalar modes, indicating that the scalar field couples differently to the metric redshift function than the gauge field.

Fig. 8 displays how the Murnaghan phantom coupling β influences the scalar spectrum. Increasing β (moving toward stronger phantom character) reduces both Re(ω) and the damping rate. Physically, larger β deepens the effective negative radial pressure ($p_r = -\rho$) and enhances the scalar-fluid contribution at intermediate radii, broadening and lowering the wave potential peak; this produces lower oscillation frequency and longer damping times. The influence on scalar QNMs is more significant than that caused by η, indicating that the Murnaghan sector plays a pivotal role in determining the scalar spectrum for the selected parameter set.

Fig. 9 reveals the sensitivity of scalar QNMs to the non-linear amplitude λ. As λ increases, both Re(ω) and the damping rate rise, resulting in the scalar modes exhibiting higher frequencies and more rapid damping. This opposite trend to β arises because λ multiplies the nonlinear $\rho^{1+1/\Gamma}$ correction in the EoS and effectively stiffens the Murnaghan fluid at moderate radii, which raises the potential peak and increases leakage into the horizon, hence larger Im(ω).The result highlights that the Murnaghan nonlinearity parameter λ provides a tunable mechanism to change both frequency and decay times.

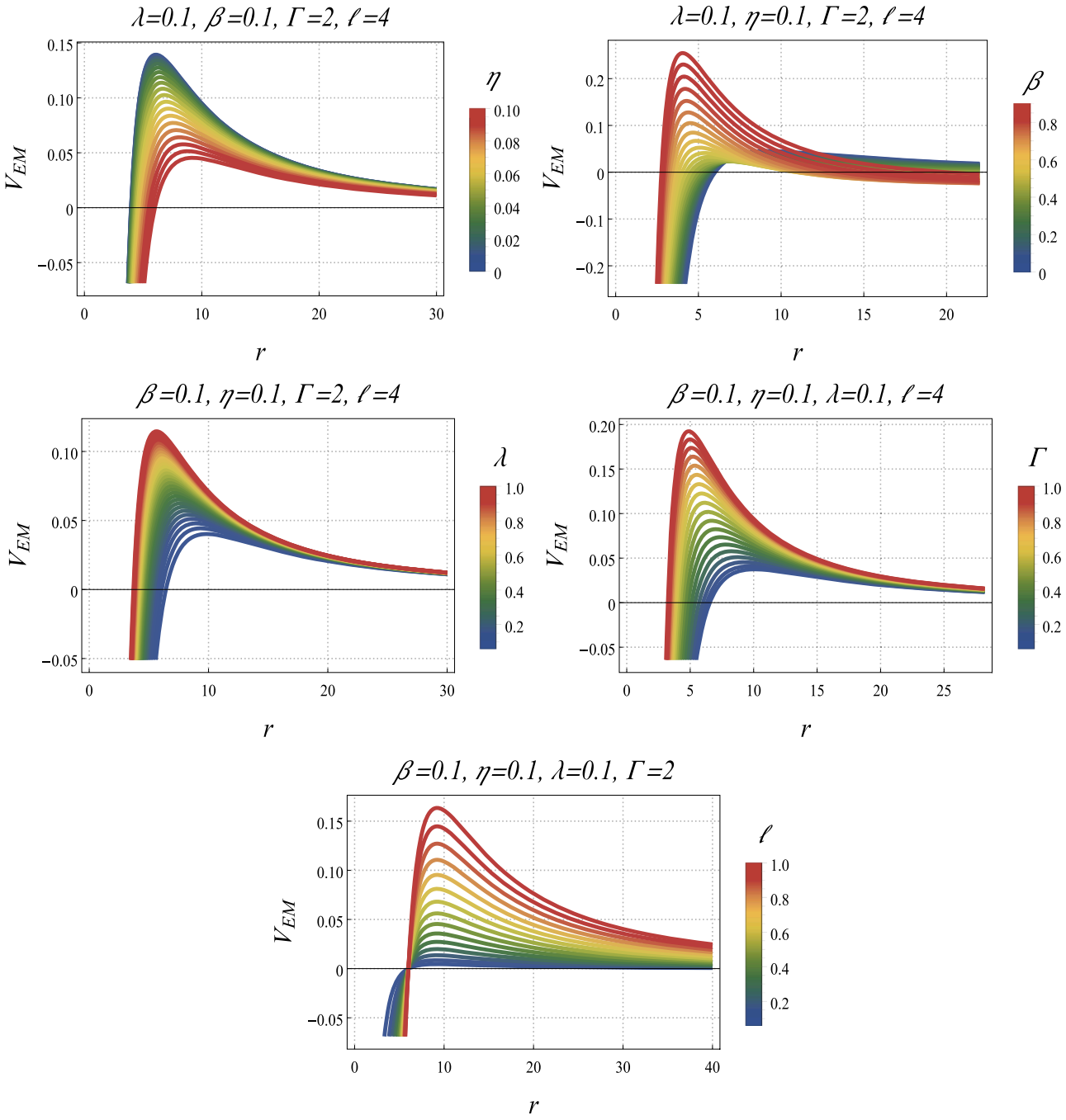

Fig. 11. electromagnetic potential $V_{EM}(r)$ as a function of the radial coordinate r for representative values of the model parameters and for several multipole numbers ℓ with $M = 1$.

Fig. 10 shows the effect of the polytropic index Γ on scalar QNMs. Increasing Γ smoothly increases Re(ω) and also increases the damping rate; however, for large Γ, the variations saturate. Physically, Γ controls how rapidly the nonlinear term in the Murnaghan EoS departs from linear behaviour: larger Γ concentrates the nonlinear corrections nearer the core and therefore modifies the effective potential in a way similar to increasing λ. The saturation at larger Γ suggests that the QNM response is controlled by the fluid profile close to the horizon for the parameter range considered.

5.4. Electromagnetic perturbations

Here, we examine electromagnetic perturbations on the spacetime solution $g_{\mu\nu}$ (6)within the tetrad formalism [146]. By employing the Bianchi identity for the electromagnetic field strength, expressed as $F_{[(a)(b)(c)]} = 0$, we arrive at the following:

$$\left(r\sqrt{g_{tt}}\,F_{(t)(\phi)}\right)_{,r} + r\sqrt{g_{rr}}\,F_{(\phi)(r),t} = 0, \tag{57}$$

$$\left(r\sqrt{g_{tt}}\,F_{(t)(\phi)}\sin\theta\right)_{,\theta} + r^2\sin\theta\,F_{(\phi)(r),t} = 0. \tag{58}$$

The conservation equation, $\eta^{(b)(c)}\left(F_{(a)(b)}\right)_{(c)} = 0$, gives

$$\left(r\sqrt{g_{tt}}\,F_{(\phi)(r)}\right)_{,r} + \sqrt{|g_{tt}|g_{rr}}\,F_{(\phi)(\theta),\theta} + r\sqrt{g_{rr}}\,F_{(t)(\phi),t} = 0. \tag{59}$$

Redefining the field perturbation as $\mathcal{F} = F_{(t)(\phi)}\sin\theta$ allows us to differentiate Eq. (59); the resulting expression is then substituted into Eqs. (57) and (58) to obtain

$$\left[\sqrt{|g_{tt}|g_{rr}^{-1}}\left(r\sqrt{|g_{tt}|}\,\mathcal{F}\right)_{,r}\right]_{,r} + \frac{|g_{tt}|\sqrt{g_{rr}}}{r}\left(\frac{\mathcal{F}_{,\theta}}{\sin\theta}\right)_{,\theta}\sin\theta - r\sqrt{g_{rr}}\,\mathcal{F}_{,tt} = 0, \tag{60}$$

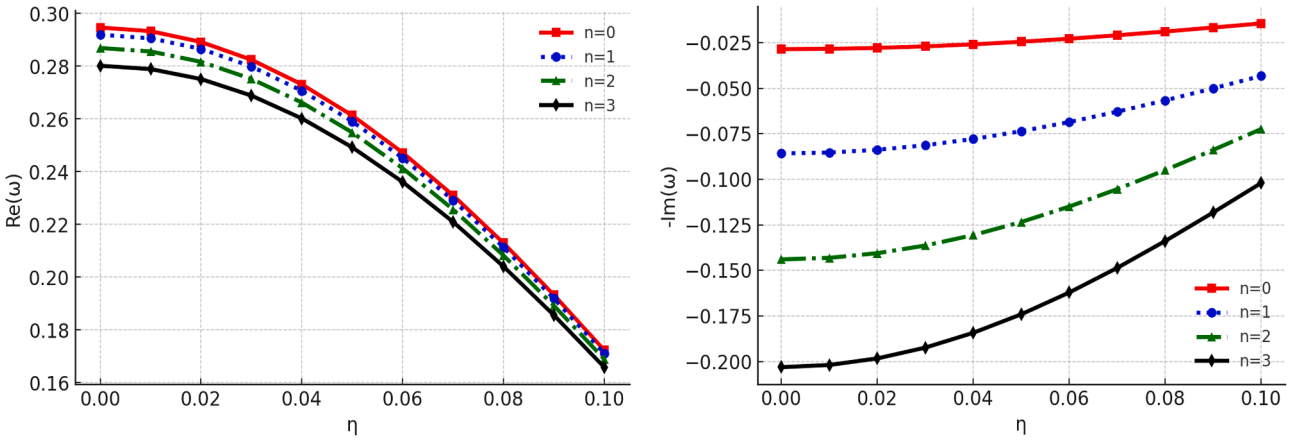

Fig. 12. Variation of the electromagnetic QNMs with respect to η with $\Gamma = 2, \beta = 0.1, \lambda = 0.1, \chi = 1$, $M = 1$ and $\ell = 4$.

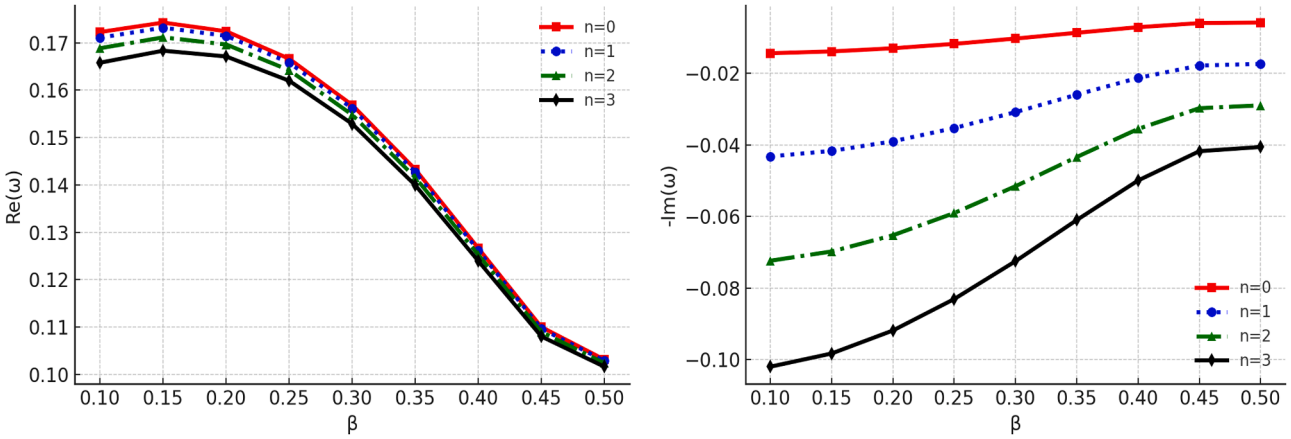

Fig. 13. Variation of the electromagnetic QNMs with respect to β with $\Gamma = 2, \eta = 0.01, \lambda = 0.1, \chi = 1$, $M = 1$ and $\ell = 4$.

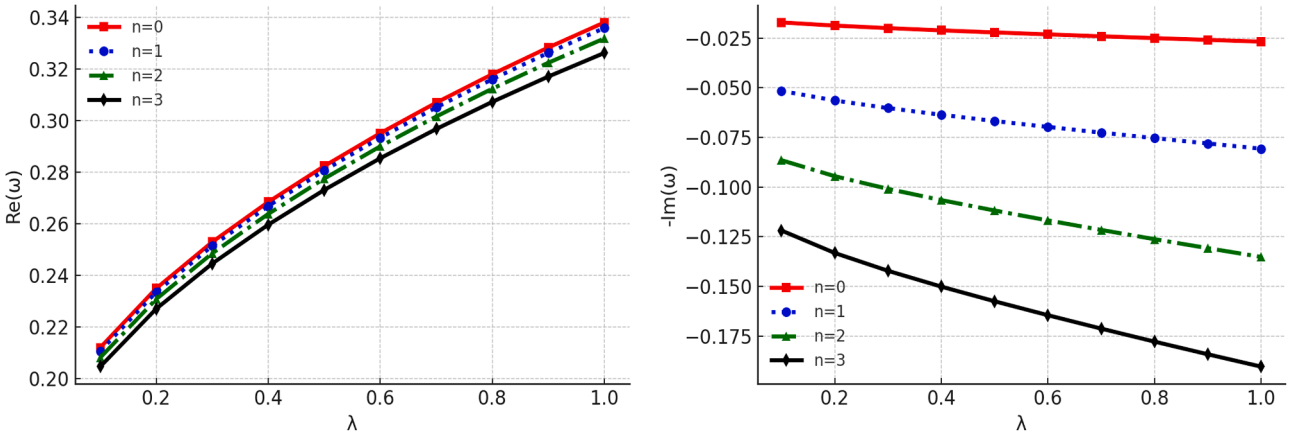

Fig. 14. Variation of the electromagnetic QNMs with respect to λ with $\Gamma = 2, \beta = 0.1, \eta = 0.01, \chi = 1$, $M = 1$ and $\ell = 4$.

Accordingly, in applying Fourier and field decompositions, respectively, $(\partial_t \to -i\omega)$ and $\mathcal{F}(r,\theta) = \mathcal{F}(r)Y_{,\theta}/\sin\theta$[2] [107], Eq. (60) can be reformulated as follows

$$\left[\sqrt{|g_{tt}|g_{rr}^{-1}}\left(r\sqrt{|g_{tt}|}\,\mathcal{F}\right)_{,r}\right]_{,r} + \omega^2 r\sqrt{g_{rr}}\,\mathcal{F} - |g_{tt}|\sqrt{g_{rr}}r^{-1}l(l+1)\,\mathcal{F} = 0. \tag{61}$$

It is noteworthy, in the light of the above considerations, that by taking $\psi_e \equiv r\sqrt{|g_{tt}|}\,\mathcal{F}$ and introducing the tortoise coordinate, the perturbation equation can be expressed in the form of a Schrödinger-like equation such as

$$\partial^2_{r_*}\psi_e + \omega^2\psi_e = V_e(r)\psi_e, \tag{62}$$

with the potential defined as

$$V_{\rm EM}(r) = |g_{tt}|\frac{\ell(\ell+1)}{r^2} \tag{63}$$

[2] Here, $Y(\theta)$ is the Gegenbauer function [108].

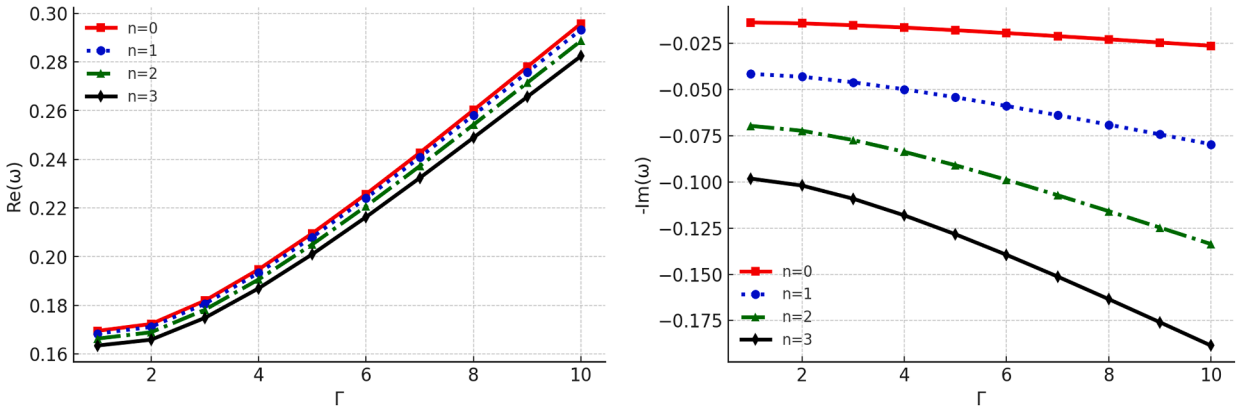

Fig. 15. Variation of the electromagnetic QNMs with respect to Γ with $\eta = 0.01, \beta = 0.1, \lambda = 0.1, \chi = 1$, $M = 1$ and $\ell = 4$.

As in the scalar case, $V_{\rm EM} \to 0$ at the horizon and decays at large distances; however, since $V_{\rm EM}$ carries no derivative terms, it loses its direct sensitivity to $F'(r)$ or $F''(r)$ and thus maintains a simpler form, closer to that of Schwarzschild, in most parameter ranges. This insight points to a generally weaker parameter-induced shape distortion observed in the electromagnetic potential plots (Fig. 11).

Physically speaking, parameters that change the redshift amplitude, most notably the global monopole parameter η, across its solid-angle deficit, and any other term that shifts $F(r)$ as a whole have the largest observable effect on $V_{\rm EM}$. From this observational fact, electromagnetic perturbations are strongly sensitive to the global monopole parameter η, which primarily generates shifts in damping and modest changes in frequency. Conversely, the Murnaghan parameter sector $\{\lambda, \Gamma, \beta, \chi\}$, in light of the electromagnetic channel, has a relatively weak effect on the QNM frequency spectrum only by indirect means. Numerically, this, in turn, implies that electromagnetic damping shows significant sensitivity to monopole variations, whereas scalar perturbations reflect stronger sensitivity to derivative-dependent Murnaghan corrections (see Tables 3, 4 and Figs. 12–15). Furthermore, graphical plots confirmed the physical observation in such a way that the electromagnetic effective potential looks appropriately Schwarzschild-like and is viewed as less structured than the scalar potential. Thus, variations in $(\lambda, \Gamma, \beta, \chi)$ affect $V_{\rm EM}$ only indirectly via the redshift factor g_{tt}; the most probable and observed driver of electromagnetic potential distortion is the monopole parameter η. Broadly speaking, electromagnetic QNMs imply smaller amplitude responses to Murnaghan-parameter variation compared to scalar QNMs.

5.5. Numerical and graphical analysis of electromagnetic perturbations and QNM spectra for the spacetime solution $g_{\mu\nu}$ (27) under systematic variation of the paramter set $\{\eta, \lambda, \beta, \Gamma\}$, employing the 3^{th}-order WKB-Padé method

To enhance our understanding of the analysis of the electromagnetic perturbation along the spacetime solution (6), the Padé accuracy method at $3^{\rm th}$-order provides QNM frequencies for the multipole number $\ell = 4$ for various parameter model values and overtones $n = 0, 1, 2, 3$. For that reason, the primary analysis is devoted to examining the numerical QNM frequencies by means of Tables 3 and 4, then to graphical behaviour through Figs. 12–15.

5.5.1. Tables 3 and 4

Table 3 provides the electromagnetic counterpart to Table 1 and shows broadly similar qualitative trends but with important quantitative differences. As η increases, the electromagnetic Re(ω) tends to decrease, and |Im(ω)| also tends to decrease, matching the behaviour in the scalar channel. However, for the parameter slices shown, the relative change in damping due to η is typically larger for electromagnetic modes than for scalar modes, reflecting that the electromagnetic effective potential (centrifugal term modulated by the redshift factor) is particularly sensitive to redshift changes induced by the monopole. The WKB-Padé uncertainty Δ estimates are small for the fundamental electromagnetic mode, reinforcing that the observed η-dependence is significant. These results suggest that monopole-induced lengthening of ringdown decay times may be more evident in electromagnetic perturbations than in scalar ones, which could be useful for channel-dependent observational diagnostics.

The electromagnetic effective potential (Eq. (63)) depends algebraically on the redshift factor and may be written as $V_{\rm EM}(r) = |g_{tt}(r)|\ell(\ell+1)/r^2$, and therefore responds primarily to bulk shifts in g_{tt} rather than to derivative-driven structure (see the discussion following Eq. (63)). For the parameter slices shown in Table 3 the monopole parameter η induces a monotonic but numerically mild change in the overall redshift at the photon sphere; consequently, as η is varied through small values (e.g. $0 \to 0.1$) the electromagnetic Re(ω) and Im(ω) display gradual, nearly linear shifts and therefore appear to "converge" to a narrow band. This behaviour does not signal a sharp phase transition but rather the dominance of the centrifugal / redshift term over derivative corrections in the electromagnetic channel for the chosen multipole and overtone range. Numerically, the apparent convergence is further supported by the small WKB-Padé uncertainty reported for the fundamental electromagnetic mode (Table 4), indicating that the observed bound is robust at the quoted precision.

Table 3 provides the electromagnetic counterpart to Table 1 and shows broadly similar qualitative trends but with important quantitative differences. As η increases, the electromagnetic Re(ω) tends to decrease, and |Im(ω)| also tends to decrease, matching the behaviour in the scalar channel. However, for the parameter slices shown, the relative change in damping due to η is typically larger for electromagnetic modes than for scalar modes, reflecting that the electromagnetic effective potential (centrifugal term modulated by the redshift factor) is particularly sensitive to redshift changes induced by the monopole. The WKB-Padé uncertainty Δ estimates are small for the fundamental electromagnetic mode, reinforcing that the observed η-dependence is significant. These results suggest that monopole-induced lengthening of ringdown decay times may be more evident in electromagnetic perturbations than in scalar ones, which could be useful for channel-dependent observational diagnostics. The electromagnetic effective potential (Eq. (63)) depends algebraically on the redshift factor and may be written as $V_{\rm EM}(r) = |g_{tt}(r)|\ell(\ell+1)/r^2$, and therefore responds primarily to bulk shifts in g_{tt} rather than to derivative-driven structure (see the discussion following Eq. (63)). For the parameter slices shown in Table 3 the monopole parameter η induces a monotonic but numerically mild change in the overall redshift at the photon sphere; consequently, as η is varied through small values (e.g. $0 \to 0.1$) the electromagnetic Re(ω) and Im(ω) display gradual, nearly linear shifts and therefore appear to "converge" to a narrow band. This behaviour does not signal

Table 1
Variation of $\ell = 4$ scalar QNMs with η (left) and β (right) for various overtones n. Left table: $\beta = 0.1$, $\lambda = 0.1, \Gamma = 2$, $\chi = 1$, and $M = 1$. Right table: $\eta = 0.1$, $\lambda = 0.1, \Gamma = 2$, $\chi = 1$, and $M = 1$.

η	n	ω	Δ
0.0	0	$0.298601 - 0.0285751\,i$	7.11395×10^{-7}
	1	$0.295918 - 0.0860784\,i$	0.0000402037
	2	$0.290971 - 0.144454\,i$	0.000119076
	3	$0.284352 - 0.203835\,i$	0.000296825
0.01	0	$0.297205 - 0.0284054\,i$	7.04499×10^{-7}
	1	$0.294541 - 0.0855664\,i$	0.0000398169
	2	$0.289628 - 0.143592\,i$	0.000117946
	3	$0.283054 - 0.202617\,i$	0.000294058
0.02	0	$0.293034 - 0.0278999\,i$	6.84106×10^{-7}
	1	$0.290427 - 0.0840408\,i$	0.0000386729
	2	$0.285617 - 0.141026\,i$	0.000114603
	3	$0.279176 - 0.198989\,i$	0.000285869
0.03	0	$0.286143 - 0.0270688\,i$	6.51092×10^{-7}
	1	$0.283629 - 0.0815333\,i$	0.0000368201
	2	$0.278987 - 0.136809\,i$	0.000109186
	3	$0.272765 - 0.193027\,i$	0.000272587
0.04	0	$0.276622 - 0.0259294\,i$	6.06872×10^{-7}
	1	$0.274235 - 0.0780959\,i$	0.000034337
	2	$0.269822 - 0.131028\,i$	0.000101918
	3	$0.263897 - 0.184855\,i$	0.000254745
0.05	0	$0.264598 - 0.0245057\,i$	5.53331×10^{-7}
	1	$0.262368 - 0.073801\,i$	0.000031328
	2	$0.258238 - 0.123806\,i$	0.0000930993
	3	$0.252684 - 0.174648\,i$	0.000233061
0.06	0	$0.250234 - 0.022828\,i$	4.92736×10^{-7}
	1	$0.248187 - 0.0687406\,i$	0.0000279192
	2	$0.244388 - 0.115298\,i$	0.0000830917
	3	$0.239266 - 0.162624\,i$	0.000208403
0.07	0	$0.233734 - 0.0209328\,i$	4.27621×10^{-7}
	1	$0.23189 - 0.0630253\,i$	0.0000242517
	2	$0.22846 - 0.105692\,i$	0.000072303
	3	$0.223822 - 0.149049\,i$	0.000181754
0.08	0	$0.215339 - 0.0188623\,i$	3.6066×10^{-7}
	1	$0.213712 - 0.0567828\,i$	0.000020475
	2	$0.210678 - 0.0952018\,i$	0.0000611669
	3	$0.206563 - 0.13423\,i$	0.000154165
0.09	0	$0.19533 - 0.0166643\,i$	2.94523×10^{-7}
	1	$0.193929 - 0.0501572\,i$	0.0000167392
	2	$0.191308 - 0.0840715\,i$	0.0000501213
	3	$0.187738 - 0.118509\,i$	0.000126707
0.1	0	$0.174032 - 0.014391\,i$	2.31732×10^{-7}
	1	$0.172858 - 0.0433064\,i$	0.0000131864
	2	$0.170654 - 0.0725672\,i$	0.0000395846
	3	$0.167639 - 0.102264\,i$	0.000100412

β	n	ω	Δ
0.1	0	$0.174032 - 0.014391\,i$	2.31732×10^{-7}
	1	$0.172858 - 0.0433064\,i$	0.0000131864
	2	$0.170654 - 0.0725672\,i$	0.0000395846
	3	$0.167639 - 0.102264\,i$	0.000100412
0.15	0	$0.175911 - 0.0138828\,i$	1.97678×10^{-7}
	1	$0.174839 - 0.0417644\,i$	0.0000109619
	2	$0.172816 - 0.0699506\,i$	0.0000329682
	3	$0.17003 - 0.09853\,i$	0.0000839512
0.2	0	$0.173885 - 0.0129874\,i$	1.56869×10^{-7}
	1	$0.172934 - 0.039059\,i$	8.74193×10^{-6}
	2	$0.171127 - 0.0653881\,i$	0.0000265137
	3	$0.16862 - 0.0920585\,i$	0.000068038
0.25	0	$0.167852 - 0.0117563\,i$	1.1371×10^{-7}
	1	$0.167028 - 0.0353466\,i$	6.71807×10^{-6}
	2	$0.165452 - 0.0591464\,i$	0.0000207298
	3	$0.163245 - 0.0832314\,i$	0.0000538764
0.3	0	$0.15782 - 0.0102686\,i$	7.31437×10^{-8}
	1	$0.157118 - 0.0308661\,i$	5.00068×10^{-6}
	2	$0.155768 - 0.0516287\,i$	0.0000158459
	3	$0.153861 - 0.0726228\,i$	0.000041921
0.35	0	$0.143967 - 0.00864503\,i$	4.07741×10^{-8}
	1	$0.14338 - 0.0259811\,i$	3.61228×10^{-6}
	2	$0.142245 - 0.043445\,i$	0.0000118024
	3	$0.140627 - 0.0610932\,i$	0.0000318417
0.4	0	$0.127067 - 0.00708613\,i$	2.33742×10^{-8}
	1	$0.126596 - 0.0212923\,i$	2.53618×10^{-6}
	2	$00.12568 - 0.0355938\,i$	8.47751×10^{-6}
	3	$0.124366 - 0.0500359\,i$	0.0000232077
0.45	0	$0.110226 - 0.00593673\,i$	2.81916×10^{-8}
	1	$0.109883 - 0.0178315\,i$	1.82984×10^{-6}
	2	$0.109212 - 0.0297861\,i$	6.16648×10^{-6}
	3	$0.108242 - 0.0418295\,i$	0.0000169626
0.5	0	$0.103265 - 0.00578303\,i$	5.95907×10^{-8}
	1	$0.103007 - 0.0173617\,i$	1.62396×10^{-6}
	2	$0.102502 - 0.0289754\,i$	5.32275×10^{-6}
	3	$0.101767 - 0.0406402\,i$	0.0000144021

Table 2
Variation of $\ell = 4$ scalar QNMs with λ (left) and Γ (right) for various overtones n. Left table: $\beta = 0.1$, $\eta = 0.1$, $\Gamma = 2$, $\chi = 1$, and $M = 1$. Right table: $\eta = 0.1$, $\lambda = 0.1$, $\beta = 0.1$, $\chi = 1$, and $M = 1$.

λ	n	ω	Δ
0.1	0	$0.214158 - 0.0172085\,i$	2.62878×10^{-7}
	1	$0.212822 - 0.0517744\,i$	0.0000140891
	2	$0.210307 - 0.086729\,i$	0.0000419057
	3	$0.206855 - 0.122181\,i$	0.000105947
0.2	0	$0.237263 - 0.0188105\,i$	2.7844×10^{-7}
	1	$0.235834 - 0.0565892\,i$	0.0000146115
	2	$0.23314 - 0.0947806\,i$	0.0000433652
	3	$0.229438 - 0.133504\,i$	0.000109592
0.3	0	$0.25536 - 0.0200828\,i$	2.89986×10^{-7}
	1	$0.253852 - 0.0604133\,i$	0.0000151315
	2	$0.251006 - 0.101177\,i$	0.0000449562
	3	$0.24709 - 0.1425\,i$	0.000113733
0.4	0	$0.270974 - 0.0212082\,i$	2.9994×10^{-7}
	1	$0.269388 - 0.0637966\,i$	0.0000157226
	2	$0.266394 - 0.106837\,i$	0.0000468714
	3	$0.262271 - 0.150463\,i$	0.000118833
0.5	0	$0.284994 - 0.0222511\,i$	3.0927×10^{-7}
	1	$0.283329 - 0.0669326\,i$	0.0000164155
	2	$0.280184 - 0.112085\,i$	0.0000491948
	3	$0.275849 - 0.157849\,i$	0.000125102
0.6	0	$0.297843 - 0.0232414\,i$	3.18502×10^{-7}
	1	$0.296096 - 0.0699109\,i$	0.0000172267
	2	$0.292793 - 0.117071\,i$	0.0000519726
	3	$0.288236 - 0.164869\,i$	0.000132655
0.7	0	$0.309755 - 0.0241943\,i$	3.27949×10^{-7}
	1	$0.307921 - 0.0727775\,i$	0.0000181646
	2	$0.304452 - 0.121872\,i$	0.0000552264
	3	$0.299663 - 0.17163\,i$	0.000141546
0.8	0	$0.320875 - 0.0251181\,i$	3.37798×10^{-7}
	1	$0.31895 - 0.0755571\,i$	0.0000192308
	2	$0.315305 - 0.126528\,i$	0.0000589566
	3	$0.310272 - 0.17819\,i$	0.00015177
0.9	0	$0.3313 - 0.026017\,i$	3.48139×10^{-7}
	1	$0.329278 - 0.0782622\,i$	0.0000204218
	2	$0.325451 - 0.131062\,i$	0.0000631452
	3	$0.320162 - 0.184579\,i$	0.000163272
1	0	$0.341099 - 0.0268929\,i$	3.58996×10^{-7}
	1	$0.338977 - 0.0808986\,i$	0.0000217292
	2	$0.33496 - 0.135481\,i$	0.0000677574
	3	$0.329407 - 0.19081\,i$	0.00017595

Table 2
continued.

Γ	n	ω	Δ
1	0	$0.171123 - 0.0138715\,i$	2.16379×10^{-7}
	1	$0.170031 - 0.041737\,i$	0.000011751
	2	$0.167977 - 0.0699219\,i$	0.0000349955
	3	$0.165161 - 0.0985135\,i$	0.0000884916
2	0	$0.174032 - 0.014391\,i$	2.31732×10^{-7}
	1	$0.172858 - 0.0433064\,i$	0.0000131864
	2	$0.170654 - 0.0725672\,i$	0.0000395846
	3	$0.167639 - 0.102264\,i$	0.000100412
3	0	$0.183722 - 0.0153918\,i$	2.53072×10^{-7}
	1	$0.182438 - 0.0463224\,i$	0.000014845
	2	$0.180028 - 0.0776327\,i$	0.0000447861
	3	$0.176737 - 0.109419\,i$	0.000113822
4	0	$0.196729 - 0.016655\,i$	2.78509×10^{-7}
	1	$0.195314 - 0.0501282\,i$	0.0000167352
	2	$0.192662 - 0.0840213\,i$	0.0000506811
	3	$0.189043 - 0.118438\,i$	0.000128984
5	0	$0.211743 - 0.0180925\,i$	3.07156×10^{-7}
	1	$0.210182 - 0.0544586\,i$	0.0000188449
	2	$0.207257 - 0.0912897\,i$	0.0000572506
	3	$0.20327 - 0.128698\,i$	0.000145865
6	0	$0.228076 - 0.0196551\,i$	3.38445×10^{-7}
	1	$0.226355 - 0.059166\,i$	0.0000211585
	2	$0.223134 - 0.0991911\,i$	0.000064456
	3	$0.218748 - 0.139851\,i$	0.000164374
7	0	$0.24528 - 0.0213085\,i$	3.71921×10^{-7}
	1	$0.243389 - 0.0641472\,i$	0.0000236577
	2	$0.239852 - 0.107553\,i$	0.0000722453
	3	$0.235041 - 0.151655\,i$	0.00018438
8	0	$0.263016 - 0.0230249\,i$	4.07161×10^{-7}
	1	$0.260946 - 0.0693185\,i$	0.0000263204
	2	$0.257079 - 0.116234\,i$	0.0000805532
	3	$0.251822 - 0.163912\,i$	0.000205719
9	0	$0.281004 - 0.0247799\,i$	4.43751×10^{-7}
	1	$0.27875 - 0.0746066\,i$	0.0000291212
	2	$0.274541 - 0.125113\,i$	0.0000893019
	3	$0.268825 - 0.176448\,i$	0.00022819
10	0	$0.299008 - 0.0265514\,i$	4.81273×10^{-7}
	1	$0.296565 - 0.079945\,i$	0.0000320314
	2	$0.292008 - 0.134077\,i$	0.0000984027
	3	$0.285823 - 0.189106\,i$	0.000251565

a sharp phase transition but rather the dominance of the centrifugal / redshift term over derivative corrections in the electromagnetic channel for the chosen multipole and overtone range. Numerically, the apparent convergence is further supported by the small WKB-Padé uncertainty reported for the fundamental electromagnetic mode (Table 4), indicating that the observed bound is robust at the quoted precision.

Table 3 provides the electromagnetic counterpart to Table 1 and shows broadly similar qualitative trends but with important quantitative differences. As η increases, the electromagnetic $\mathrm{Re}(\omega)$ tends to decrease, and $|\mathrm{Im}(\omega)|$ also tends to decrease, matching the behaviour in the scalar channel. However, for the parameter slices shown, the relative change in damping due to η is typically larger for electromagnetic modes than for scalar modes, reflecting that the electromagnetic effective potential (centrifugal term modulated by the redshift factor) is particularly sensitive to redshift changes induced by the monopole. The WKB-Padé uncertainty Δ estimates are small for the fundamental electromagnetic mode, reinforcing that the observed η-dependence is significant. These results suggest that monopole-induced lengthening of ringdown decay times may be more evident in electromagnetic perturbations than in scalar ones, which could be useful for channel-dependent observational diagnostics.

The electromagnetic effective potential (Eq. (63)) depends algebraically on the redshift factor and may be written as $V_{\mathrm{EM}}(r) =$

Table 3
Variation of $\ll = 4$ electromagnetic QNMs with η (left) and β (right) for various overtones n. Left table: $\beta = 0.1$, $\lambda = 0.1$, $\Gamma = 2$, $\chi = 1$, and $M = 1$. Right table: $\eta = 0.1$, $\lambda = 0.1$, $\Gamma = 2$, $\chi = 1$, and $M = 1$.

η	n	ω	Δ
0.0	0	$0.294613 - 0.0284712\,i$	7.14539×10^{-7}
	1	$0.291885 - 0.0857735\,i$	0.000041737
	2	$0.286861 - 0.143962\,i$	0.000124427
	3	$0.280144 - 0.203166\,i$	0.00031104
0.01	0	$0.293245 - 0.0283024\,i$	7.07605×10^{-7}
	1	$0.290537 - 0.085264\,i$	0.0000413316
	2	$0.285548 - 0.143105\,i$	0.000123233
	3	$0.278877 - 0.201954\,i$	0.000308106
0.02	0	$0.28916 - 0.0277994\,i$	6.87102×10^{-7}
	1	$0.28651 - 0.0837461\,i$	0.0000401329
	2	$0.281626 - 0.140551\,i$	0.000119702
	3	$0.27509 - 0.198343\,i$	0.000299425
0.03	0	$0.282408 - 0.0269726\,i$	6.53911×10^{-7}
	1	$0.279854 - 0.081251\,i$	0.0000381925
	2	$0.275141 - 0.136353\,i$	0.000113983
	3	$0.268828 - 0.192407\,i$	0.000285352
0.04	0	$0.273076 - 0.025839\,i$	6.09457×10^{-7}
	1	$0.270652 - 0.0778303\,i$	0.0000355936
	2	$0.266172 - 0.130599\,i$	0.000106315
	3	$0.260163 - 0.184272\,i$	0.000266465
0.05	0	$0.261286 - 0.0244223\,i$	5.55638×10^{-7}
	1	$0.259022 - 0.073556\,i$	0.0000324474
	2	$0.254832 - 0.12341\,i$	0.000097022
	3	$0.2492 - 0.174109\,i$	0.000243536
0.06	0	$0.247196 - 0.0227526\,i$	4.94736×10^{-7}
	1	$0.245118 - 0.0685192\,i$	0.0000288871
	2	$0.241265 - 0.11494\,i$	0.0000864901
	3	$0.236074 - 0.162137\,i$	0.0002175
0.07	0	$0.230998 - 0.0208662\,i$	4.293×10^{-7}
	1	$0.229128 - 0.0628295\,i$	0.0000250621
	2	$0.22565 - 0.105375\,i$	0.0000751545
	3	$0.220952 - 0.148619\,i$	0.000189408
0.08	0	$0.212927 - 0.018805\,i$	3.62021×10^{-7}
	1	$0.211279 - 0.056614\,i$	0.0000211297
	2	$0.208204 - 0.0949285\,i$	0.000063476
	3	$0.204037 - 0.133858\,i$	0.000160384
0.09	0	$0.193255 - 0.0166163\,i$	2.95584×10^{-7}
	1	$0.191836 - 0.0500157\,i$	0.000017247
	2	$0.189181 - 0.0838422\,i$	0.0000519175
	3	$0.185569 - 0.118196\,i$	0.000131563
0.1	0	$0.172294 - 0.0143521\,i$	2.32522×10^{-7}
	1	$0.171106 - 0.0431916\,i$	0.0000135623
	2	$0.168876 - 0.0723809\,i$	0.0000409186
	3	$0.165827 - 0.10201\,i$	0.000104034

β	n	ω	Δ
0.1	0	$0.172294 - 0.0143521\,i$	2.32522×10^{-7}
	1	$0.171106 - 0.0431916\,i$	0.0000135623
	2	$0.168876 - 0.0723809\,i$	0.0000409186
	3	$0.165827 - 0.10201\,i$	0.000104034
0.15	0	$0.174292 - 0.0138499\,i$	1.98542×10^{-7}
	1	$0.173208 - 0.0416674\,i$	0.0000112501
	2	$0.171163 - 0.0697931\,i$	0.000033984
	3	$0.168348 - 0.0983157\,i$	0.0000867114
0.2	0	$0.172445 - 0.0129607\,i$	1.5759×10^{-7}
	1	$0.171485 - 0.0389803\,i$	8.94606×10^{-6}
	2	$0.169661 - 0.0652601\,i$	0.0000272353
	3	$0.167131 - 0.0918842\,i$	0.0000700101
0.25	0	$0.166643 - 0.0117351\,i$	1.14124×10^{-7}
	1	$0.165812 - 0.0352839\,i$	6.85084×10^{-6}
	2	$0.164223 - 0.059044\,i$	0.0000212085
	3	$0.162 - 0.0830915\,i$	0.0000552031

Table 3
continued.

0.3	0	$0.156878 - 0.0102514\,i$	7.31909×10^{-8}
	1	$0.156172 - 0.0308149\,i$	5.07952×10^{-6}
	2	$0.154813 - 0.0515446\,i$	0.0000161447
	3	$0.152894 - 0.0725072\,i$	0.0000427724
0.35	0	$0.143304 - 0.00863001\,i$	4.05335×10^{-8}
	1	$0.142714 - 0.0259362\,i$	3.65493×10^{-6}
	2	$0.141573 - 0.0433709\,i$	0.0000119804
	3	$0.139946 - 0.0609906\,i$	0.0000323725
0.4	0	$0.12666 - 0.00707241\,i$	2.3029×10^{-8}
	1	$0.126187 - 0.0212512\,i$	2.55702×10^{-6}
	2	$0.125267 - 0.0355255\,i$	8.57905×10^{-6}
	3	$0.123946 - 0.0499406\,i$	0.0000235296
0.45	0	$0.110004 - 0.00592488\,i$	2.78896×10^{-8}
	1	$0.10966 - 0.0177958\,i$	1.83904×10^{-6}
	2	$0.108987 - 0.0297265\,i$	6.22386×10^{-6}
	3	$0.108014 - 0.0417457\,i$	0.0000171574
0.5	0	$0.103123 - 0.0057724\,i$	5.93581×10^{-8}
	1	$0.102865 - 0.0173296\,i$	1.62655×10^{-6}
	2	$0.10236 - 0.0289215\,i$	5.35435×10^{-6}
	3	$0.101624 - 0.0405638\,i$	0.0000145202

$|g_{tt}(r)|\ell(\ell+1)/r^2$, and therefore responds primarily to bulk shifts in g_{tt} rather than to derivative-driven structure (see the discussion following Eq. (63)). For the parameter slices shown in Table 3 the monopole parameter η induces a monotonic but numerically mild change in the overall redshift at the photon sphere; consequently, as η is varied through small values (e.g. $0 \to 0.1$) the electromagnetic $\mathrm{Re}(\omega)$ and $\mathrm{Im}(\omega)$ display gradual, nearly linear shifts and therefore appear to "converge" to a narrow band. This behaviour does not signal a sharp phase transition but rather the dominance of the centrifugal / redshift term over derivative corrections in the electromagnetic channel for the chosen multipole and overtone range. Numerically, the apparent convergence is further supported by the small WKB-Padé uncertainty reported for the fundamental electromagnetic mode (Table 4), indicating that the observed bound is robust at the quoted precision.

Table 4 shows how the Murnaghan sector modifies electromagnetic QNMs. The trends track those seen for scalar modes but with reduced amplitude in some directions: increasing λ and Γ generally raise $\mathrm{Re}(\omega)$ and increase $|Im(\omega)|$, while variations in β have a weaker but still noticeable effect on $\mathrm{Re}(\omega)$. Compared to scalar modes, electromagnetic modes are less sensitive to the detailed pressure-derivative structure of the Murnaghan fluid and more sensitive to the redshift-modifying aspects of the metric; thus the λ/Γ-induced shifts are mainly mediated through changes of $F(r)$ rather than through derivative-sensitive terms. As for scalars, WKB Δ is small for the lowest multipoles and overtones; for higher overtones the uncertainties become comparable to parameter-induced shifts.

5.5.2. Figs. 12–15

Fig. 12: electromagnetic modes shows a greater sensitivity of $-\mathrm{Im}(\omega)$ to η compared to scalar modes. As η increases, the damping decreases more significantly, resulting in longer-lived electromagnetic ringing. This confirms that the electromagnetic perturbations (with potential $V_e \sim |g_{tt}|\ell(\ell+1)/r^2$) react strongly to changes in the redshift due to the solid-angle deficit introduced by the global monopole. The trend indicates that global-monopole effects can be more visible in electromagnetic signal decay than in scalar channels for the same parameter shifts.

Fig. 13 illustrates that varying β has a modest impact on electromagnetic frequencies: the real part of ω, denoted as $\mathrm{Re}(\omega)$, experiences only a slight change, while the damping exhibits a gradual variation, albeit less pronounced than that observed for scalar modes. This suggests that while the Murnaghan phantom fluid produces large metric corrections for the scalar effective potential (which contains derivative terms), the

Table 4
Variation of $\ell = 4$ electromagnetic QNMs with λ (left) and Γ (right) for various overtones n. Left table: $\beta = 0.1$, $\eta = 0.1$, $\Gamma = 2$, $\chi = 1$, and $M = 1$. Right table: $\eta = 0.1$, $\lambda = 0.1$, $\beta = 0.1$, $\chi = 1$, and $M = 1$.

λ	n	ω	Δ
0.1	0	$0.212103 - 0.0171659\,i$	2.64142×10^{-7}
	1	$0.210752 - 0.0516487\,i$	0.0000144829
	2	$0.208207 - 0.0865253\,i$	0.0000432805
	3	$0.204717 - 0.121904\,i$	0.00010966
0.2	0	$0.235031 - 0.018766\,i$	2.79919×10^{-7}
	1	$0.233586 - 0.0564581\,i$	0.0000150159
	2	$0.230861 - 0.0945682\,i$	0.0000447687
	3	$0.227118 - 0.133215\,i$	0.000113377
0.3	0	$0.25299 - 0.0200368\,i$	2.91583×10^{-7}
	1	$0.251464 - 0.0602778\,i$	0.000015547
	2	$0.248586 - 0.100957\,i$	0.0000463964
	3	$0.244627 - 0.142202\,i$	0.000117616
0.4	0	$0.268482 - 0.0211607\,i$	3.01594×10^{-7}
	1	$0.266879 - 0.0636568\,i$	0.0000161512
	2	$0.263851 - 0.106611\,i$	0.0000483589
	3	$0.259683 - 0.150156\,i$	0.000122848
0.5	0	$0.282391 - 0.0222022\,i$	3.10934×10^{-7}
	1	$0.280707 - 0.0667884\,i$	0.0000168595
	2	$0.277527 - 0.111852\,i$	0.0000507405
	3	$0.273145 - 0.157533\,i$	0.000129282
0.6	0	$0.295134 - 0.0231908\,i$	3.20134×10^{-7}
	1	$0.293367 - 0.0697618\,i$	0.0000176884
	2	$0.290027 - 0.11683\,i$	0.0000535871
	3	$0.285423 - 0.164542\,i$	0.000137032
0.7	0	$0.306945 - 0.0241419\,i$	3.29512×10^{-7}
	1	$0.305091 - 0.0726231\,i$	0.0000186459
	2	$0.301583 - 0.121622\,i$	0.0000569197
	3	$0.296745 - 0.171291\,i$	0.000146148
0.8	0	$0.317968 - 0.0250637\,i$	3.39256×10^{-7}
	1	$0.31602 - 0.0753967\,i$	0.0000197338
	2	$0.312336 - 0.126269\,i$	0.0000607379
	3	$0.307252 - 0.177838\,i$	0.000156626
0.9	0	$0.328297 - 0.0259604\,i$	3.49459×10^{-7}
	1	$0.326252 - 0.0780953\,i$	0.000020948
	2	$0.322384 - 0.130792\,i$	0.0000650223
	3	$0.317043 - 0.184213\,i$	0.000168405
1	0	$0.338002 - 0.0268338\,i$	3.60146×10^{-7}
	1	$0.335857 - 0.0807246\,i$	0.0000222801
	2	$0.331798 - 0.1352\,i$	0.0000697373
	3	$0.32619 - 0.190428\,i$	0.000181381

Γ	n	ω	Δ
1	0	$0.16946 - 0.0138361\,i$	2.17347×10^{-7}
	1	$0.168355 - 0.0416326\,i$	0.0000120817
	2	$0.166276 - 0.0697525\,i$	0.0000361541
	3	$0.163429 - 0.098283\,i$	0.0000916238
2	0	$0.172294 - 0.0143521\,i$	2.32522×10^{-7}
	1	$0.171106 - 0.0431916\,i$	0.0000135623
	2	$0.168876 - 0.0723809\,i$	0.0000409186
	3	$0.165827 - 0.10201\,i$	0.000104034
3	0	$0.181855 - 0.0153486\,i$	2.53744×10^{-7}
	1	$0.180555 - 0.0461949\,i$	0.0000152717
	2	$0.178117 - 0.0774257\,i$	0.0000463129
	3	$0.174789 - 0.109137\,i$	0.000117978
4	0	$0.194702 - 0.0166068\,i$	2.79074×10^{-7}
	1	$0.193269 - 0.049986\,i$	0.0000172196
	2	$0.190585 - 0.0837903\,i$	0.000052425
	3	$0.186925 - 0.118123\,i$	0.000133741
5	0	$0.209533 - 0.0180387\,i$	3.07603×10^{-7}
	1	$0.207952 - 0.0543\,i$	0.0000193936
	2	$0.204992 - 0.091032\,i$	0.0000592375
	3	$0.200959 - 0.128346\,i$	0.000151293

Table 4
continued.

6	0	$0.225668 - 0.0195953\,i$	3.38754×10^{-7}
	1	$0.223925 - 0.0589894\,i$	0.0000217782
	2	$0.220665 - 0.0989041\,i$	0.000066711
	3	$0.216227 - 0.139459\,i$	0.000170544
7	0	$0.242661 - 0.0212421\,i$	3.72067×10^{-7}
	1	$0.240746 - 0.0639512\,i$	0.0000243546
	2	$0.237166 - 0.107234\,i$	0.0000747927
	3	$0.232298 - 0.15122\,i$	0.00019136
8	0	$0.260177 - 0.0229515\,i$	4.07115×10^{-7}
	1	$0.258081 - 0.0691021\,i$	0.0000271001
	2	$0.254166 - 0.115882\,i$	0.0000834154
	3	$0.248847 - 0.163431\,i$	0.00021357
9	0	$0.27794 - 0.0246993\,i$	4.43483×10^{-7}
	1	$0.275657 - 0.0743688\,i$	0.0000299887
	2	$0.271396 - 0.124726\,i$	0.0000924987
	3	$0.265612 - 0.175919\,i$	0.000236968
10	0	$0.295716 - 0.0264634\,i$	4.80753×10^{-7}
	1	$0.293241 - 0.0796852\,i$	0.0000329908
	2	$0.288627 - 0.133655\,i$	0.00010195
	3	$0.282368 - 0.188528\,i$	0.000261318

purely centrifugal electromagnetic potential is mainly sensitive to the redshift factor and less to radial profile derivatives.

Fig. 14: An increase in λ results in an upward shift of electromagnetic Re(ω) and a slight increase in damping. This behaviour qualitatively reflects the scalar trend but exhibits a reduced magnitude. This phenomenon occurs because the stiffening of the fluid alters g_{tt}, thereby affecting the centroid of the centrifugal barrier. However, effects that are sensitive to derivatives remain absent in the electromagnetic axial sector.

Fig. 15 illustrates the weak dependence of electromagnetic modes on Γ, exhibiting a slight upward trend in both Re(ω) and $-$Im(ω). The saturation behaviour observed in scalar fields for large Γ is also present here, albeit to a lesser extent. The observation made alongside the scalar panels reinforces the interpretation that the Murnaghan sector serves as the primary factor influencing frequency shifts. In contrast, the monopole parameter exerts a more significant control over damping within the electromagnetic channel. This again underscores that electromagnetic modes primarily sample the global redshift rather than the local derivative structure.

To summarise, the electromagnetic and scalar perturbations respond differently to parameter variations: their QNM spectra show systematic changes in the real part (oscillation frequency) and the imaginary part (damping rate) when the coupling set is varied, keeping the multipole ℓ fixed while scanning overtone number n. Roughly speaking, this can be presented as

- The scalar and electromagnetic perturbation channels respond to spacetime and matter changes through two distinct mechanisms. The scalar effective potential $V_s(r)$ contains metric-derivative terms and therefore is highly sensitive to local changes in the metric derivatives $F'(r), F''(r)$ induced by the Murnaghan fluid parameters $(\lambda, \Gamma, \beta, \chi)$. The electromagnetic axial potential $V_{\rm EM}(r)$, by contrast, is dominated by the centrifugal term $\propto |g_{tt}|\ell(\ell+1)/r^2$ and lacks derivative-dependent structure; it therefore responds mainly to global redshift changes (e.g., the monopole parameter η). These mechanistic differences explain the qualitative and quantitative trends observe and quantitative trends observedved in Figs. 7–15.
- The trends visible in Figs. 7–15 are quantitatively corroborated by the QNM tables: (i) scalar-mode frequencies and damping show

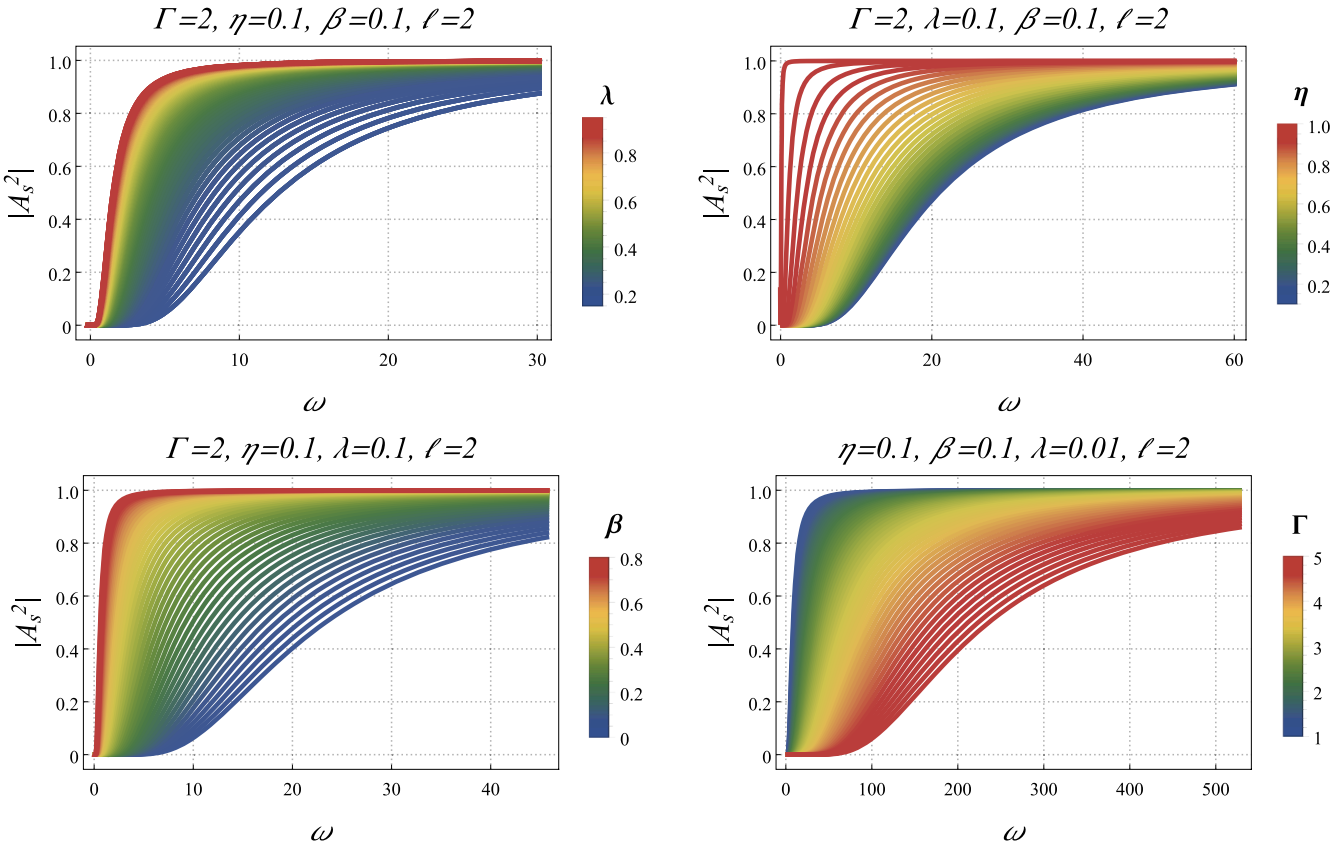

Fig. 16. Rigorous upper and lower bounds on the electromagnetic greybody factor as functions of frequency, computed for $M = 1$ and representative values of the model parameters.

larger fractional shifts when λ, Γ, β are varied; (ii) EM-mode damping exhibits the strongest sensitivity to η; and (iii) the Padé error estimates (reported in the tables) are sufficiently small for fundamental modes to render the above monotonic relations robust. These table-to-figure agreements strengthen the physical interpretation given above.

6. Greybody bounds from electromagnetic perturbation

This section addresses the derivation and analysis of greybody bounds caused by an electromagnetic perturbation governed by $V_{\rm EM}$ on the spacetime solution. In light of previous QNM electromagnetic spectra, third-order Padé analysis has demonstrated that the Murnaghan sector, particularly the global monopole parameter, significantly influences the frequency spectrum. Therefore, we intend to further investigate this finding by revealing how these parameters are shaping the greybody bounds. To this end, it is paramount to employ an analytical and numerical method disclosing rigorous bounds. In particular, analytical methods were first pioneered by Visser [135] and subsequently refined by Boonserm and Visser [136]. On the other hand, numerous studies like Boonserm et al. [137], Yang et al. [129], Grey et al. [138], Ngampitipan et al. [139], and others [137,140–144] have explored these limits in even greater detail.

At this stage, we aim to quantify the influence of the parameter set $\{M, \eta, \beta, \lambda, \Gamma, \chi\}$ on the transmission coefficients by solving Maxwell's equations within the background metric $g_{\mu\nu}$ and systematically varying these parameters. To achieve this, we utilise Eqs. (57) and (58) introduced in the previous section. This method reformulates the problem as a single-channel scattering issue, where the effective potential corresponds exactly to the electromagnetic potential $V_{\rm EM}$

$$V_{\rm EM}(r) = \frac{\ell(\ell+1)F(r)}{r^2}. \tag{64}$$

where ℓ is the multipole number.

Subsequently, we apply the effective potential identified previously to examine the lower bound on the greybody factor in the essence of our BH solution. Concerning the work of Visser [135] and Boonserm and Visser [136], the appropriate method to determine this stringent limit is given by:

$$A_g^2 \geq \operatorname{sech}^2\left(\frac{1}{2\omega}\int_{-\infty}^{\infty}|V_{\rm EM}|\frac{dr}{F(r)}\right), \tag{65}$$

where A_g^2 denotes the transmission coefficient T in this context.

In addition, to accommodate the influence of the cosmological horizon, we adjust the boundary conditions as shown by Boonserm et al. [145]. The modified boundary conditions are:

$$A_g^2 \geq A_s^2 = \operatorname{sech}^2\left(\frac{1}{2\omega}\int_{r_H}^{R_H}\frac{|V_{\rm EM}|}{F(r)}dr\right) = \operatorname{sech}^2\left(\frac{A_l}{2\omega}\right), \tag{66}$$

where we define

$$A_l = \int_{r_H}^{R_H}\frac{|V_{\rm EM}|}{F(r)}dr = \int_{r_H}^{R_H}\left|\frac{\ell(\ell+1)}{r^2}\right|dr. \tag{67}$$

Here, r_H is the event horizon and R_H is the cosmological horizon of the BH. This specification supplies a rigorous lower bound on the grey-body factors relative to the BH solution.

Fig. 16 shows sech-based rigorous lower bounds on the greybody transmission factor for electromagnetic and massless scalar fields. The Murnaghan parameters enter the exponent via the integrand $V_{\rm eff}|/F(r)$: raising λ or Γ increases the effective potential and hence lowers the transmission bound, while increasing η modifies $F(r)$ and the curvature near the peak, producing upward shifts of the bound over certain radial ranges. These trends agree with the QNM behaviour: parameters that enhance the potential peak (larger λ, Γ) produce stronger damping (larger Im) and reduced transmission, and the monopole η partially counteracts these effects in the slices shown.

7. Conclusion

We constructed and analysed static, spherically symmetric BH solutions sourced by a global monopole (strength η) coupled to a nonlinear Murnaghan scalar fluid parametrised by $(\lambda, \beta, \Gamma, \chi)$. The monopole acted principally as a deficit-angle modifier: increasing η shifted the metric function $F(r)$ downward at small and intermediate radii and pushed the outer horizon r_h outward, while the Murnaghan sector sculpted the near-horizon slope and curvature where larger λ tended to stiffen the near-horizon profile, larger Γ reduced intermediate-radius hypergeometric corrections (modestly decreasing r_h), and larger β lowered the near-horizon profile and shifted the metric crossing inward without producing inner horizons within the non-phantom window considered. These geometric changes were tightly linked to local stress-energy behaviour: the NEC was restored at large r but could be violated close to the horizon for parameter choices that amplified intermediate-radius scalar-fluid contributions (notably larger β); DEC violations were broader and occurred when transverse pressures became strongly negative (promoted by decreasing λ or increasing β); and the SEC proved the most fragile, being easily violated by modest changes in β or Γ. In short, the monopole set the global geometry and horizon size, while the Murnaghan fluid controlled localised near-horizon deviations and parameter-dependent EC violations that constrained theoretical viability.

The sparsity and Hawking-emission diagnostics showed consistent, parameter-dependent departures from Schwarzschild behaviour. We parameterised sparsity by $\tilde{\eta}(r_h)$ and benchmarked it against the Schwarzschild reference $\tilde{\eta}_{\rm Sch} \simeq 73.49$. Larger η produced an overall downward vertical shift of $\tilde{\eta}(r_h)$ at small and moderate r_h, bringing the curves closer to-and in many slices below the Schwarzschild baseline, which signalled less sparse (more continuous) emission. Increasing β steepened the falloff of $\tilde{\eta}(r_h)$ and, for $\beta \gtrsim 1/3$, often drove the curves below the Schwarzschild reference at moderate radii. The nonlinearity λ compressed the family of curves toward the Schwarzschild line (larger $\lambda \Rightarrow$ smaller vertical spread), whereas smaller λ fanned the family outward and produced the largest departures; increasing Γ induced a slight downward shift at intermediate r_h followed by saturation. Collectively, these trends indicated that monopole and phantom-character effects could render Hawking emission qualitatively less sparse, while β, λ, Γ controlled how abrupt or gradual that transition appeared.

The scalar and electromagnetic QNM spectra provided complementary, channel-dependent fingerprints of the monopole and Murnaghan sectors. Using a third-order WKB-Padé scheme for multipole $\ell = 4$ and overtones $n = 0, 1, 2, 3$ (with Padé uncertainty Δ small for $n = 0, 1$ and increasing for larger n), we found that increasing η monotonically lowered $\mathrm{Re}(\omega)$ and reduced $|\mathrm{Im}(\omega)|$ in both channels (modes oscillated more slowly and lived longer), with electromagnetic damping exhibiting larger relative sensitivity to η because the electromagnetic axial potential primarily sampled global redshift. By contrast, increasing the Murnaghan nonlinearity amplitude λ or the polytropic index Γ raised $\mathrm{Re}(\omega)$ and increased damping (a higher/narrower effective potential $\Rightarrow$ higher frequency and stronger leakage), while increasing the phantom-like coupling β lowered both $\mathrm{Re}(\omega)$ and damping (a broader, lower potential peak). Scalar QNMs were therefore markedly more sensitive to $\lambda, \Gamma, \beta, \chi$ via metric derivatives F', F'', whereas electromagnetic QNMs primarily probed η. The observed saturation of QNM shifts at large Γ indicated that the response was controlled by the fluid structure close to the horizon for the parameter range considered, and the small Padé errors for fundamental modes rendered the qualitative monotonic relations robust for the modes most relevant to observational prospects.

Rigorous greybody (sech-based) lower bounds and their relation to QNMs produced a consistent dynamical picture. The Murnaghan parameters entered the transmission exponent through the effective-potential structure (appearing in integrands $\sim V_{\rm eff}/F(r)$ within the sech-bound formulation): raising λ or Γ increased the effective potential and therefore lowered the sech-based transmission bound (reduced transmission), consistent with the concurrent increase in QNM damping; in-

creasing η modified the redshift and peak curvature and yielded upward shifts of the transmission bound in selected radial ranges, in line with the monopole-driven reduction in damping. These matched trends-higher potential $\Leftrightarrow$ larger $|\mathrm{Im}(\omega)|$ and smaller transmission; larger η $\Leftrightarrow$ smaller $|\mathrm{Im}(\omega)|$ and often larger transmission demonstrated internal consistency between linear perturbation leakage and scattering properties. The greybody and sparsity diagnostics together implied that certain Murnaghan-monopole parameter combinations led to qualitatively distinct Hawking-emission characteristics (less sparse spectra and modified transmissivity), albeit with the important caveat that astrophysical detectability of such signatures would be challenging and might be more viable in analogue gravity experiments.

Data availability statement

This manuscript has no associated data or the data will not be deposited. (There is no observational data related to this article. The necessary calculations and graphic discussion can be made available on request.)

Author statment

The authors are very thankful to you and the referee for giving such useful comments for our article. These comments/suggestions will enhance the quality of the paper. We have addressed all the comments as indicated in the reviewed report, which has been also included in the revised version of the article. The main changes have been highlighted in the manuscript in blue color. We hope that the revised manuscript will meet the journal publication requirements.

Declaration of competing interest

The authors declare that they have no known competing financial interests or personal relationships that could have appeared to influence the work reported in this paper.

CRediT authorship contribution statement

Y. Sekhmani: Writing - review & editing, Writing - original draft, Visualization, Validation, Software, Methodology, Investigation, Formal analysis, Conceptualization; **S. K. Maurya:** Writing - review & editing, Writing - original draft, Visualization, Validation, Supervision, Investigation, Formal analysis, Conceptualization; **J. Rayimbaev:** Writing - review & editing, Writing - original draft, Visualization, Validation, Resources, Investigation, Formal analysis, Conceptualization; **Akram Ali:** Writing - review & editing, Writing - original draft, Visualization, Resources, Funding acquisition, Formal analysis, Conceptualization; **M. K. Jasim:** Writing - review & editing, Writing - original draft, Visualization, Validation, Investigation, Formal analysis, Conceptualization; **I. Ibragimov:** Writing - review & editing, Writing - original draft, Visualization, Formal analysis, Conceptualization; **S. Muminov:** Writing - review & editing, Visualization, Validation, Investigation, Formal analysis, Conceptualization.

Acknowledgments

The authors extend their appreciation to the Deanship of Research and Graduate Studies at King Khalid University, Saudi Arabia for funding this work through a Large Research Project under grant number RGP2/3/46. The authors MKJ and SKM is thankful to UoN administration for continuous support and encouragement for the research works.

References

[1] K. Schwarzschild, Sitzungsber, Preuss. Akad. Wiss. Berlin (Math. Phys.) 1916 (1916) 189–196.
[2] D. Finkelstein, Phys. Rev. 110 (1958) 965–967.
[3] M.D. Kruskal, Phys. Rev. 119 (1960) 1743–1745.
[4] R. Abbott, et al., [LIGO Scientific and Virgo], Phys. Rev. D 102 (4) (2020) 043015.
[5] R. Abbott, et al., [LIGO Scientific and Virgo], Phys. Rev. Lett. 125 (10) (2020) 101102.
[6] J. Liu, H. Zhang, A.W. Howard, Z. Bai, Y. Lu, R. Soria, S. Justham, X. Li, Z. Zheng, T. Wang, et al., Nature 575 (7784) (2019) 618–621.
[7] K. Akiyama, et al., [Event Horizon Telescope], Astrophys. J. Lett. 875 (2019) L1.
[8] K. Akiyama, et al., [Event Horizon Telescope], Astrophys. J. Lett. 875 (1) (2019) L2.
[9] K. Akiyama, et al., [Event Horizon Telescope], Astrophys. J. Lett. 875 (1) (2019) L3.
[10] K. Akiyama, et al., [Event Horizon Telescope], Astrophys. J. Lett. 875 (1) (2019) L4.
[11] K. Akiyama, et al., [Event Horizon Telescope], Astrophys. J. Lett. 875 (1) (2019) L5.
[12] K. Akiyama, et al., [Event Horizon Telescope], Astrophys. J. Lett. 875 (1) (2019) L6.
[13] K. Akiyama, et al., [Event Horizon Telescope], Astrophys. J. Lett. 910 (1) (2021) L12.
[14] K. Akiyama, et al., [Event Horizon Telescope], Astrophys. J. Lett. 910 (1) (2021) L13.
[15] K. Akiyama, et al., [Event Horizon Telescope], Astrophys. J. Lett. 957 (2) (2023) L20.
[16] K. Akiyama, et al., [Event Horizon Telescope], Astrophys. J. Lett. 930 (2) (2022) L12.
[17] K. Akiyama, et al., [Event Horizon Telescope], Astrophys. J. Lett. 930 (2) (2022) L13.
[18] K. Akiyama, et al., [Event Horizon Telescope], Astrophys. J. Lett. 930 (2) (2022) L14.
[19] K. Akiyama, et al., [Event Horizon Telescope], Astrophys. J. Lett. 930 (2) (2022) L15.
[20] K. Akiyama, et al., [Event Horizon Telescope], Astrophys. J. Lett. 930 (2) (2022) L16.
[21] K. Akiyama, et al., [Event Horizon Telescope], Astrophys. J. Lett. 964 (2) (2024) L26.
[22] A. Einstein, Science 84 (1936) 506–507.
[23] K.S. Virbhadra, G.F.R. Ellis, Phys. Rev. D 62 (2000) 084003.
[24] V. Perlick, Living Rev. Rel. 7 (2004) 9. https://doi.org/10.12942/lrr-2004-9
[25] P.V.P. Cunha, C.A.R. Herdeiro, Gen. Rel. Grav. 50 (4) (2018) 42.
[26] R. Kumar, S.G. Ghosh, Astrophys. J. 892 (2020) 78.
[27] S.G. Ghosh, R. Kumar, S.U. Islam, JCAP 03 (2021) 056.
[28] M. Afrin, R. Kumar, S.G. Ghosh, Mon. Not. Roy. Astron. Soc. 504 (4) (2021) 5927–5940.
[29] S.G. Ghosh, M. Afrin, Astrophys. J. 944 (2) (2023) 174.
[30] Y. Mizuno, Z. Younsi, C.M. Fromm, O. Porth, M. De Laurentis, H. Olivares, H. Falcke, M. Kramer, L. Rezzolla, Nature Astron. 2 (7) (2018) 585–590.
[31] D. Psaltis, Gen. Rel. Grav. 51 (10) (2019) 137.
[32] A. Stepanian, S. Khlghatyan, V.G. Gurzadyan, Eur. Phys. J. Plus 136 (1) (2021) 127.
[33] Z. Younsi, D. Psaltis, F. Özel, Astrophys. J. 942 (1) (2023) 47.
[34] V. Perlick, O.Y. Tsupko, Phys. Rep. 947 (2022) 1–39.
[35] R.K. Walia, S.G. Ghosh, S.D. Maharaj, Astrophys. J. 939 (2) (2022) 77.
[36] S. Vagnozzi, R. Roy, Y.D. Tsai, L. Visinelli, M. Afrin, A. Allahyari, P. Bambhaniya, D. Dey, S.G. Ghosh, P.S. Joshi, et al., Class. Quant. Grav. 40 (16) (2023) 165007.
[37] A. Belhaj, Y. Sekhmani, Gen. Rel. Grav. 54 (2) (2022) 17.
[38] A. Belhaj, Y. Hassouni, M. Oualaid, Y. Sekhmani, Int. J. Mod. Phys. D 32 (04) (2023) 2350016.
[39] Y. Sekhmani, D.J. Gogoi, R. Myrzakulov, G.G. Luciano, J. Rayimbaev, Class. Quant. Grav. 41 (18) (2024) 185002.
[40] Y. Sekhmani, S. Zare, L.M. Nieto, H. Hassanabadi, K. Boshkayev, JHEAp 47 (2025) 100389.
[41] A. Al-Badawi, Y. Sekhmani, K. Boshkayev, Phys. Dark Univ. 48 (2025) 101865.
[42] M. Fathi, Y. Sekhmani, Eur. Phys. J. C 85 (5) (2025) 477.
[43] Y. Sekhmani, H. Ali, S.G. Ghosh, K. Boshkayev, JHEAp 49 (2026) 100425.
[44] Y. Sekhmani, K. Boshkayev, M. Azreg-Aïnou, S.K. Maurya, M. Altanji, A. Urazalina, [arXiv:2509.16782 [gr-qc]].
[45] V. Vertogradov, A. Övgün, R.C. Pantig, Int. J. Geom. Meth. Mod. Phys. 22 (10) (2025) 2540001.
[46] B.P. Abbott, et al., [LIGO Scientific and Virgo], Phys. Rev. Lett. 116 (2016) 061102.
[47] E. Berti, V. Cardoso, A.O. Starinets, Class. Quant. Grav. 26 (2009) 163001.
[48] R.A. Konoplya, A. Zhidenko, Rev. Mod. Phys. 83 (2011) 793–836.
[49] M. Chabab, H.E. Moumni, S. Iraoui, K. Masmar, Eur. Phys. J. C 76 (12) (2016) 676.
[50] S. Chakraborty, K. Chakravarti, S. Bose, S. SenGupta, Phys. Rev. D 97 (10) (2018) 104053.
[51] A. Ishibashi, H. Kodama, Prog. Theor. Phys. 110 (2003) 901–919.
[52] H. Kodama, A. Ishibashi, Prog. Theor. Phys. 110 (2003) 701–722.
[53] H. Kodama, A. Ishibashi, Prog. Theor. Phys. 111 (2004) 29–73.
[54] H. Kodama, R.A. Konoplya, A. Zhidenko, Phys. Rev. D 79 (2009) 044003.
[55] R.A. Konoplya, A. Zhidenko, Nucl. Phys. B 777 (2007) 182–202.
[56] R.A. Konoplya, A. Zhidenko, Phys. Rev. D 77 (2008) 104004.
[57] R.A. Konoplya, A. Zhidenko, Phys. Rev. D 78 (2008) 104017.
[58] R.A. Konoplya, A. Zhidenko, Phys. Rev. Lett. 103 (2009) 161101.
[59] M. Shibata, H. Yoshino, Phys. Rev. D 81 (2010) 104035.
[60] H. Witek, M. Zilhao, L. Gualtieri, V. Cardoso, C. Herdeiro, A. Nerozzi, U. Sperhake, Phys. Rev. D 82 (2010) 104014.

[61] A. Jawad, S. Chaudhary, M. Yasir, A. Övgün, İ. Sakallı, Int. J. Geom. Meth. Mod. Phys. 20 (08) (2023) 2350129.
[62] A. Övgün, İ. Sakallı, H. Mutuk, Int. J. Geom. Meth. Mod. Phys. 18 (10) (2021) 2150154.
[63] Y. Sekhmani, D.J. Gogoi, Int. J. Geom. Meth. Mod. Phys. 20 (09) (2023) 2350160.
[64] D.J. Gogoi, R. Karmakar, U.D. Goswami, Int. J. Geom. Meth. Mod. Phys. 20 (01) (2023) 2350007.
[65] M. Barriola, A. Vilenkin, Gravitational field of a global monopole, Phys. Rev. Lett. 63 (341) (1989).
[66] A. Vilenkin, E.P.S. Shellard, 1994, Cosmic Strings and Other Topological Defects, Cambridge University Press
[67] F.D. Mazzitelli, C.O. Loust, Phys. Rev. D 43 (468) (1991).
[68] D. Harari, C. Loust, Phys. Rev. D 42 (2626) (1990).
[69] U. Nucamendi, M. Salgado, D. Sudarsky, Phys. Rev. Lett. 84 (2000) 3037.
[70] A.S. Goldhaber, Phys. Rev. Lett. 63 (1989) 2158.
[71] J. Man, H. Cheng, Phys. Rev. D 87 (044002) (2013).
[72] T.H. Lee, Class. Quant. Grav. 27 (2010) 247001.
[73] J.P.M. Graça, H.S. Vieira, Eur. Phys. J. C 76 (254) (2016).
[74] M.E.X. Guimarães, Mod. Phys. Lett. A 27 (1250177) (2012).
[75] H. Koyama, A. Tomimatsu, Phys. Rev. D 64 (044014) (2001).
[76] H. Yu, Phys. Rev. D 65 (087502) (2002).
[77] J.P.M. Graça, H.S. Vieira, V.B. Bezerra, Gen. Relat. Grav. 48 (38) (2016).
[78] F.D. Murnaghan, Proc. Natl. Acad. Sci. USA 30 (1944) 244–247.
[79] S.P. Weppner, J.P. McKelvey, K.D. Thielen, A.K. Zielinski, Mon. Not. R. Astron. Soc. 452 (2015) 1375–1393.
[80] P.K.S. Dunsby, O. Luongo, M. Muccino, V. Pillay, Phys. Dark Univ. 46 (2024) 101563.
[81] A.N. Seenivasan, S. Chakrabarti, B.R. Majhi, Phys. Rev. D 107 (10) (2023) 104027.
[82] Y. Sekhmani, S.K. Maurya, J. Rayimbaev, M. Altanji, I. Ibragimov, A. Landry, S. Muminov, [arXiv:2509.16728 [gr-qc]].
[83] F. Ahmed, İ. Sakallı, A. Al-Badawi, Phys. Lett. B 864 (2025) 139448.
[84] F. Ahmed, A. Al-Badawi, İ. Sakallı, Phys. Dark Univ. 49 (2025) 101988.
[85] F. Ahmed, A. Al-Badawi, İ. Sakallı, S. Kanzi, Phys. Dark Univ. 48 (2025) 101907.
[86] A. Al-Badawi, İ. Sakallı, S. Kanzi, Annals Phys. 412 (2020) 168026.
[87] İ. Sakallı, A. Al-Badawi, B. Pourhassan, A.B. Brzo, Mod. Phys. Lett. A 40 (33) (2025) 2550150.
[88] D. Krimans, S. Putterman, Phys. Fluids 35 (8) 086114. (2023), AIP Publishing.
[89] I. Cho, H.C. Kim, Phys. Rev. D 95 (8) (2017) 084052.
[90] S. Capozziello, E. Battista, S. De Bianchi, Phys. Rev. D 112 (4) (2025) 044009. https://doi.org/10.1103/ybjp-8w2w
[91] S. De Bianchi, S. Capozziello, E. Battista, Found. Phys. 55 (3) (2025) 36. https://doi.org/10.1007/s10701-025-00848-z
[92] Z.L. Wang, E. Battista, Eur. Phys. J. C 85 (3) (2025) 304. https://doi.org/10.1140/epjc/s10052-025-13833-7
[93] S. Capozziello, S. De Bianchi, E. Battista, Phys. Rev. D 109 (10) (2024) 104060. [arXiv:2404.17267 [gr-qc]]. https://doi.org/10.1103/PhysRevD.109.104060
[94] G. Mustafa, A. Alimova, F. Atamurotov, A.A. Ibraheem, P. Channuie, G. Bahaddinova, Eur. Phys. J. C 85 (7) (2025) 741.
[95] B. Turimov, S. Usanov, Y. Khamroev, Phys. Dark Univ. 48 (2025) 101876.
[96] B. Turimov, S. Urinov, I. Mardiev, S. Usanov, M. Akylbayev, R. Kenzhebekova, https://doi.org/10.1007/s40065-025-00573-5
[97] O. Yunusov, B. Turimov, Y. Khamroev, S. Usanov, F. Turaev, M. Kuliyeva, Annals Phys. 481 (2025) 170151.
[98] B. Mashhoon, 1983, Proceedings of the Third Marcel Grossmann Meeting on General Relativity, 599–608
[99] S. Iyer, C.M. Will, Print-86-0935 (WASH.U.,ST.LOUIS).
[100] S. Iyer, C.M. Will, Phys. Rev. D 35 (1987) 3621.
[101] R.A. Konoplya, Phys. Rev. D 68 (2003) 024018.
[102] J. Matyjasek, M. Opala, Phys. Rev. D 96 (2) (2017) 024011.
[103] R.A. Konoplya, A. Zhidenko, A.F. Zinhailo, Class. Quant. Grav. 36 (2019) 155002.
[104] R.A. Konoplya, A. Zhidenko, Rev. Mod. Phys. 83 (2011) 793–836.
[105] S. Chandrasekhar, J.L. Friedman, Astrophys. J. 175 (1972) 379–405.
[106] M. Bouhmadi-López, S. Brahma, C.Y. Chen, P. Chen, D.h. Yeom, JCAP 07 (2020) 066.
[107] S. Chandrasekhar, 1991, Selected Papers, Volume 6: The Mathematical Theory of Black Holes and of Colliding Plane Waves, University of Chicago Press, Chicago.
[108] M. Abramowitz, I.A. Stegun, Handbook of Mathematical Functions (1964). Dover, New York.
[109] T.W.B. Kibble, J. Phys. A 9 (1976) 1387–1398.
[110] M. Goodband, M. Hindmarsh, Phys. Lett. B 370 (1996) 29–36.
[111] C.P. Burgess, Ann. Rev. Nucl. Part. Sci. 57 (2007) 329–362.
[112] L. Herrera, N.O. Santos, Phys. Rep. 286 (1997) 53–130.
[113] R.L. Bowers, E.P.T. Liang, Astrophys. J. 188 (1974) 657–665.
[114] R. Chan, L. Herrera, N.O. Santos, Mon. Not. Roy. Astron. Soc. 265 (3) (1993) 533–544.
[115] R.G. Cai, D.W. Pang, A. Wang, Phys. Rev. D 70 (2004) 124034.
[116] Y. Verbin, Phys. Rev. D 106 (2) (2022) 2.
[117] R.R. Caldwell, Phys. Lett. B 545 (2002) 23–29.
[118] S. Nojiri, S.D. Odintsov, Phys. Rev. D 72 (2005) 023003.
[119] E. Babichev, V. Dokuchaev, Y. Eroshenko, Phys. Rev. Lett. 93 (2004) 021102.
[120] D. Bertacca, N. Bartolo, S. Matarrese, Adv. Astron. 2010 (2010) 904379.
[121] A. Barros, C. Romero, Gen. Rel. Grav. 30 (1998) 495–506.
[122] J. Preskill, A. Vilenkin, Phys. Rev. D 47 (1993) 2324–2342.
[123] F. Rahaman, M. Kalam, K.A. Rahman, Acta Phys. Polon. B 40 (2009) 1575–1590.
[124] H.M. Haddad, M.H. Seçuk, Ö. Delice, Nucl. Phys. B 1018 (2025) 117097.
[125] R.C. Tolman, Phys. Rev. 55 (1939) 364–373.
[126] J.R. Oppenheimer, G.M. Volkoff, Phys. Rev. 55 (1939) 374–381.
[127] L. Herrera, N.O. Santos, Phys. Rep. 286 (1997) 53–130.
[128] M. Abramowitz, I.A. Stegun, Handbook of Mathematical Functions (1965). Dover, New York.
[129] Y. Yang, D. Liu, A. Övgün, Z.W. Long, Z. Xu, Phys. Rev. D 107 (6) (2023) 064042.
[130] V.V. Kiselev, Class. Quant. Grav. 20 (2003) 1187.
[131] E.A. Kontou, K. Sanders, Class. Quant. Grav. 37 (2020) 193001.
[132] D.N. Page, Phys. Rev. D 13 (1976) 198.
[133] F. Gray, S. Schuster, A. Van-Brunt, M. Visser, Class. Quant. Grav. 33 (2016) 115003.
[134] Y. Sekhmani, B. Hazarika, P. Phukon, A. Landry, S.K. Maurya, J. Rayimbaev, ArXiv:2410.18247.
[135] M. Visser, Phys. Rev. A 59 (1999) 427.
[136] P. Boonserm, M. Visser, Phys. Rev. D 78 (2008) 101502.
[137] P. Boonserm, T. Ngampitipan, P. Wongjun, Eur. Phys. J. C 78 (2018) 492.
[138] F. Gray, M. Visser, Universe 4 (2018) 93.
[139] T. Ngampitipan, P. Boonserm, Int. J. Mod. Phys. D 22 (2013) 1350058.
[140] A. Chowdhury, N. Banerjee, Phys. Lett. B 805 (2020) 135417.
[141] Y.G. Miao, Z.M. Xu, Phys. Lett. B 772 (2017) 542.
[142] Y. Liu, Eur. Phys. J. C 82 (2022) 1054.
[143] S. Barman, Eur. Phys. J. C 80 (2020) 50.
[144] H. Xu, M.H. Yung, Phys. Lett. B 794 (2019) 77.
[145] P. Boonserm, T. Ngampitipan, P. Wongjun, Eur. Phys. J. C 79 (2019) 330.
[146] S. Chandrasekhar, Selected Papers of S. Chandrasekhar. Volume 6: The mathematical theory of black holes and of colliding plane waves (1991).